

Crystal Structure and Superconductivity of $\text{YBa}_2\text{Cu}_3\text{O}_{7-x}$

by

Brent A. Howe

A Thesis Submitted in Partial Fulfillment of the

Requirements for the Degree of

Master of Science

in

Physics

Minnesota State University, Mankato

Mankato, Minnesota

July 2014

Crystal Structure and Superconductivity of $\text{YBa}_2\text{Cu}_3\text{O}_{7-x}$

Brent A. Howe

This thesis has been examined and approved by the following members of the student's committee on May 7, 2014.

Dr. Youwen Xu, Advisor

Dr. Sungwon S. Kim, Committee Member

Dr. Hai-Sheng Wu, Committee Member

Abstract

Crystal Structure and Superconductivity of $\text{YBa}_2\text{Cu}_3\text{O}_{7-x}$

Brent A. Howe

Master of Science in Physics

Minnesota State University, Mankato

2014

The crystal structure and superconducting properties of samples of $\text{YBa}_2\text{Cu}_3\text{O}_{7-x}$ with oxygen contents $0.21 \leq x \leq 0.67$ were investigated. The crystal structure and magnetic properties change with oxygen content. All samples were found to have orthorhombic crystal structure. The lattice parameters a and c were observed to monotonically increase while b nearly monotonically decreases with decreasing oxygen content. The unit cell volume increases with decreasing oxygen content as well. The critical temperature, T_c , and the superconducting volume fraction of the samples decreased with decreasing oxygen content.

Contents

1	Introduction	1
1.1	Motivation for This Study	1
1.2	Early Developments in Superconductivity	1
1.3	General Properties of Superconductivity	2
1.3.1	BCS Theory	7
1.4	Type I and Type II Superconductors	9
1.5	High-Temperature Superconductors	9
1.6	$\text{YBa}_2\text{Cu}_3\text{O}_{7-x}$	11
1.7	Crystal Structure	13
1.8	X-ray Diffraction	16
2	Experimental Procedures	19
2.1	Sample Synthesis	19
2.1.1	The Original Sample	19
2.1.2	The Oxygen-Deficient Samples	20
2.2	X-ray Diffraction	24
2.3	Magnetic Measurements	25
3	Results	27
3.1	Samples Synthesized	27
3.2	Crystal Structure	29
3.3	Superconducting Transition Temperature	39
4	Discussion	49
4.1	Crystal Structure	49
4.2	Superconducting Properties	51

5 Conclusion	54
---------------------	-----------

A Material List	59
------------------------	-----------

List of Figures

1	Crystal structure of $\text{YBa}_2\text{Cu}_3\text{O}_7$	12
2	A crystal unit cell.	13
3	Illustration of the (100) and (222) crystal planes.	14
4	Diagram of the Bragg Law	17
5	Schematic of X-ray diffractometer utilizing Bragg-Brentano geometry.	24
6	X-ray Diffraction pattern of sample BH-5-YBCO with composition $\text{YBa}_2\text{Cu}_3\text{O}_7$	30
7	X-ray Diffraction pattern of sample BH-5-YBCO-14 with composition $\text{YBa}_2\text{Cu}_3\text{O}_{6.79}$	31
8	X-ray Diffraction pattern of sample BH-5-YBCO-15 with composition $\text{YBa}_2\text{Cu}_3\text{O}_{6.65}$	32
9	X-ray Diffraction pattern of sample BH-5-YBCO-2 with composition $\text{YBa}_2\text{Cu}_3\text{O}_{6.54}$	33
10	X-ray Diffraction pattern of sample BH-5-YBCO-8 with composition $\text{YBa}_2\text{Cu}_3\text{O}_{6.46}$	34
11	X-ray Diffraction pattern with indexed peaks of sample BH-5-YBCO-6 with composition $\text{YBa}_2\text{Cu}_3\text{O}_{6.33}$	35
12	Lattice parameters (a) a and b , and (b) c of $\text{YBa}_2\text{Cu}_3\text{O}_{7-x}$ as a function of oxygen composition $7 - x$	37
13	Unit cell volume, V , versus oxygen composition $7 - x$	38
14	Magnetic moment measurements for sample BH-5-YBCO with composition $\text{YBa}_2\text{Cu}_3\text{O}_7$	41
15	Magnetic moment measurements for sample BH-5-YBCO-14 with composition $\text{YBa}_2\text{Cu}_3\text{O}_{6.79}$	42

16	Magnetic moment measurements for sample BH-5-YBCO-15 with composition $\text{YBa}_2\text{Cu}_3\text{O}_{6.65}$	43
17	Magnetic moment measurements for sample BH-5-YBCO-2 with composition $\text{YBa}_2\text{Cu}_3\text{O}_{6.54}$	44
18	Magnetic moment measurements for sample BH-5-YBCO-8 with composition $\text{YBa}_2\text{Cu}_3\text{O}_{6.46}$	45
19	Magnetic moment measurements for sample BH-5-YBCO-6 with composition $\text{YBa}_2\text{Cu}_3\text{O}_{6.33}$	46
20	Superconducting transition temperature, T_c , plotted as a function of oxygen composition, $7 - x$, for samples of $\text{YBa}_2\text{Cu}_3\text{O}_{7-x}$	48
21	X-ray diffraction peaks (006), (020), and (200) in samples of $\text{YBa}_2\text{Cu}_3\text{O}_{7-x}$ are shown for samples with oxygen content 7.00, 6.79, 6.65, 6.54, 6.46, and 6.33 between $46^\circ < 2\theta < 49^\circ$	50

List of Tables

1	The seven crystal systems	15
2	Summary of box furnace settings for production of oxygen deficient samples $\text{YBa}_2\text{Cu}_3\text{O}_{7-x}$	28
3	Lattice parameters and unit cell volume for oxygen-deficient samples of $\text{YBa}_2\text{Cu}_3\text{O}_{7-x}$	36
4	Superconducting transition temperatures for oxygen-deficient samples of $\text{YBa}_2\text{Cu}_3\text{O}_{7-x}$	47
5	List of starting materials used for the synthesis of $\text{YBa}_2\text{Cu}_3\text{O}_7$ and for X-ray diffraction measurements.	59

Acknowledgements

My most sincere gratitude goes to my advisor, Dr. Youwen Xu, for her knowledge, guidance, and patience through the research, the experimentation, and the writing of this thesis. I also want to thank my graduate committee members Dr. Hai-Sheng Wu and Dr. Kim for their advice on my thesis.

Many thanks go to Mr. Michael Peters for helping acquire and operate laboratory equipment as well as Ms. Cindy Flitter for always happily assisting me in the Physics Department office. I am grateful to Dr. R.W. McCallum and K. Dennis for allowing us to use the Quantum Design Magnetometer in Ames National Laboratory to measure the magnetic properties of my samples, and their help interpreting some of the results. I would like to thank Dr. Michael Lusch of the Chemistry department as well as Dr. Penny Knoblich and Mr. Anthony Kopari, both of the Biology department, for their assistance in acquiring liquid nitrogen, .

I am eternally grateful for the enduring love and support from my wife, Ashley. She has made many sacrifices so that I could pursue my education in order to have a career in physics.

1 Introduction

1.1 Motivation for This Study

A great deal of research has been done to determine how the structural and magnetic properties affect the mechanisms of superconductivity in $\text{YBa}_2\text{Cu}_3\text{O}_{7-x}$. Despite extensive research on $\text{YBa}_2\text{Cu}_3\text{O}_{7-x}$ spanning nearly three decades, there are still inconsistencies between studies. Therefore, it is important that further research be conducted to resolve those inconsistencies. In a recent paper by Biscaras et al. [1], magnetization measurements were performed on oxygen-deficient YBCO samples in normal state in order to study the interchange between hole doping and magnetic properties. The intention of this study is to synthesize samples of $\text{YBa}_2\text{Cu}_3\text{O}_{7-x}$ and determine how the crystal structure and critical temperature, T_c , change with oxygen content as the first stage for studying the normal state of the samples in the future. In doing this, we will compare results of this study with those of past studies and create a starting point that complements the work by Biscaras et al. Crystal structures of the samples were determined by using X-ray diffraction technique, while magnetic moment measurements were made to determine T_c of each sample.

1.2 Early Developments in Superconductivity

Superconductivity is a phenomenon where a material loses all electrical resistance and becomes perfectly diamagnetic below a certain temperature. In 1911, Heike Kamerlingh Onnes first observed superconductivity in Hg wire after finding that resistivity dropped sharply to an immeasurable value upon cooling the metal to 4.2 K [2]. The discovery of superconductivity earned Onnes the 1913 Nobel Prize in Physics. In 1933, Walther Meissner and Robert Ochsenfeld found that magnetic fields are com-

pletely expelled from the interior of superconductors [3]. This property is called the Meissner effect and it established that superconductors are not just perfect conductors. The two key properties of superconductors - the expulsion of magnetic fields and perfect conductivity - were explained phenomenologically through the London theory developed by Fritz and Heinz London in 1935 [4]. In 1950, Ginzburg and Landau [5] developed a phenomenological theory that successfully explained macroscopic properties of superconductivity. It was not until 1957 that Bardeen, Cooper, and Schrieffer established a fundamental microscopic quantum theory explaining superconductivity [6]. The work for the appropriately named BCS theory earned the trio the 1972 Nobel Prize.

1.3 General Properties of Superconductivity

An electric field \vec{E} in a metal establishes a current. The current density \vec{J} and the electric field \vec{E} are related by Ohm's Law:

$$\vec{J} = \sigma \vec{E}, \tag{1}$$

where σ is the electrical conductivity. The reciprocal of conductivity is electrical resistivity ρ . The charge carriers in metals are electrons that are in conduction bands, which are partially filled energy bands, so they are called conduction electrons. Resistance of electrical conduction in metals is caused intrinsically by collisions between electrons and discrete vibrational modes in crystal lattices (phonons) and extrinsically by collisions between conduction electrons and imperfections as well as impurities in the crystal lattice [7]. The resistances from these types of collisions are largely independent of each other. They are described by the empirical expression for net

resistivity called Matthiessen's rule [8]:

$$\rho = \rho_L + \rho_i, \quad (2)$$

where ρ_L is the resistivity due to electron-phonon scattering and ρ_i is the resistivity from imperfections. In general, resistivity decreases with decreasing temperature in conductors.

A superconductor exhibits zero resistance for direct currents, an ordered state of electron pairs is responsible for the supercurrent. Conductivity $\sigma \rightarrow \infty$ for finite \vec{J} , $\vec{E} \rightarrow 0$. Electrical conduction is not described by Ohm's Law in superconductors. Instead, In the absence of an applied magnetic field, certain materials become superconducting when the temperature is lowered to a specific value called the critical temperature, T_c . The superconducting state disappears when the temperature of the material is raised above T_c .

Within a bulk superconductor, the magnetic induction $\vec{B} = 0$. The expulsion of magnetic fields does not come as a natural consequence of perfect conductivity. This can be shown by first examining Newton's second law in a perfect conductor, within which charge carriers with charge e and mass m are in an electric field \vec{E} and, thus, experience a force

$$-e\vec{E} = m\frac{d\vec{v}}{dt}. \quad (3)$$

The current density \vec{J} is defined as

$$\vec{J} = -ne\vec{v}, \quad (4)$$

where n is the density of conduction electrons. Since $\vec{v} = -\vec{J}/ne$, we have

$$e\vec{E} = \frac{m}{ne} \frac{\partial \vec{J}}{\partial t}. \quad (5)$$

Faraday's law states that

$$\vec{\nabla} \times \vec{E} = -\frac{\partial \vec{B}}{\partial t} \quad (6)$$

Substituting \vec{E} from (5) into Faraday's law, we obtain

$$\frac{m}{ne^2} \left(\vec{\nabla} \times \frac{\partial \vec{J}}{\partial t} \right) = -\frac{\partial \vec{B}}{\partial t}. \quad (7)$$

Using Ampère's law

$$\vec{\nabla} \times \vec{B} = \mu_0 \vec{J}, \quad (8)$$

and taking the time derivative of (8), We obtain

$$\vec{\nabla} \times \frac{\partial \vec{B}}{\partial t} = \mu_0 \frac{\partial \vec{J}}{\partial t}. \quad (9)$$

Substituting $\partial \vec{J}/\partial t = (1/\mu_0)\vec{\nabla} \times \partial \vec{B}/\partial t$ into (7) we find that

$$\frac{m}{ne^2} \vec{\nabla} \times \left(\frac{1}{\mu_0} \vec{\nabla} \times \frac{\partial \vec{B}}{\partial t} \right) = \frac{m}{\mu_0 ne^2} \vec{\nabla} \times \left(\vec{\nabla} \times \frac{\partial \vec{B}}{\partial t} \right) = -\frac{\partial \vec{B}}{\partial t}. \quad (10)$$

With the fact that

$$\vec{\nabla} \times \left(\vec{\nabla} \times \frac{\partial \vec{B}}{\partial t} \right) = \vec{\nabla} \cdot \left(\vec{\nabla} \cdot \frac{\partial \vec{B}}{\partial t} \right) - \nabla^2 \frac{\partial \vec{B}}{\partial t}, \quad (11)$$

and that

$$\vec{\nabla} \cdot \left(\frac{\partial \vec{B}}{\partial t} \right) = \frac{\partial}{\partial t} (\vec{\nabla} \cdot \vec{B}) = 0, \quad (12)$$

we have

$$-\frac{m}{\mu_0 n e^2} \nabla^2 \frac{\partial \vec{B}}{\partial t} = -\frac{\partial \vec{B}}{\partial t}. \quad (13)$$

rearranging Equation (13), we find that

$$\nabla^2 \frac{\partial \vec{B}}{\partial t} = \frac{\mu_0 n e^2}{m} \frac{\partial \vec{B}}{\partial t} = \frac{1}{\lambda^2} \frac{\partial \vec{B}}{\partial t}, \quad (14)$$

where λ is defined as

$$\lambda^2 = \frac{m}{\mu_0 n e^2}. \quad (15)$$

The solution to Equation (14) is

$$\frac{\partial \vec{B}(z)}{\partial t} = \frac{\partial \vec{B}(0)}{\partial t} e^{-z/\lambda}, \quad (16)$$

where the constant λ is the penetration depth and z is the distance from the surface of the conductor. This result implies \vec{B} is constant of time in the interior of the perfect conductor, but not necessarily zero. If a perfect conductor was in a magnetic field and then reached a perfect conducting state, that magnetic flux is maintained inside the material. In a superconductor, the magnetic flux density is always zero. Fritz and Heinz London developed the phenomenological theory that explained the Meissner effect. Using n_s as the superconducting electron density and J_s as the superconducting current density, Equation (5) becomes

$$\vec{E} = \frac{m}{n_s e^2} \frac{\partial \vec{J}_s}{\partial t}. \quad (17)$$

This is the first London equation. Then, Equation (7) becomes

$$\frac{m}{n_s e^2} \left(\vec{\nabla} \times \frac{\partial \vec{J}_s}{\partial t} \right) = -\frac{\partial \vec{B}}{\partial t}. \quad (18)$$

This result can be rewritten as

$$\frac{\partial}{\partial t} \left[\frac{m}{n_s e^2} \left(\vec{\nabla} \times \vec{J}_s \right) + \vec{B} \right] = 0. \quad (19)$$

Choosing the solution

$$\frac{m}{n_s e^2} \left(\vec{\nabla} \times \vec{J}_s \right) + \vec{B} = 0, \quad (20)$$

leads to the second London equation:

$$-\frac{m}{n_s e^2} \left(\vec{\nabla} \times \vec{J}_s \right) = \vec{B}. \quad (21)$$

Together with $\vec{J}_s = \frac{1}{\mu_0} \vec{\nabla} \times \vec{B}$, one finds that

$$\nabla^2 \vec{B} = \frac{\mu_0 n_s e^2}{m} \vec{B} = \frac{1}{\lambda_L^2} \vec{B}, \quad (22)$$

where λ_L is the London penetration depth and is defined as

$$\lambda_L^2 = \frac{m}{\mu_0 n_s e^2}. \quad (23)$$

The solution to the differential equation in (22) is

$$\vec{B}(z) = \vec{B}(0) e^{-z/\lambda_L}. \quad (24)$$

The difference between this result and (16) for perfect conductors is that the magnetic

field which penetrates the superconductor drops off exponentially. Thus, not only $\partial\vec{B}/\partial t = 0$, but $\vec{B} = 0$ at all times inside the superconductor. Values of the London penetration depth have been found to be on the order of 100 nm [9]. On the surface of a superconductor, currents are formed which generate a magnetic field to exactly cancel any effect the external applied magnetic field has inside the superconductor.

The expulsion of magnetic fields is a bulk property of a superconducting material. Within a magnetic material, the magnetic flux density B , the applied magnetic field strength H_a , and the magnetization M are related by

$$B = \mu_0(H_a + M). \quad (25)$$

Since $\vec{B} = 0$ inside a superconductor, Equation (25) gives us

$$M = -H_a, \quad (26)$$

and the magnetic susceptibility by:

$$\chi = \frac{dM}{dH_a} = -1. \quad (27)$$

1.3.1 BCS Theory

The BCS theory developed by Bardeen, Cooper and Schrieffer is the foundation of the microscopic quantum theory of superconductivity. According to the BCS theory, an electron-phonon interaction causes a net attraction between electrons that results in the formation of pairs of electrons of opposite spin and momentum. The electron-phonon interaction starts when one electron moves through a crystal lattice and deforms it as a result of the Coulomb attraction. The deformed lattice creates an

area of greater positive charge, so it is energetically favorable for a second electron to move closer to this area of greater positive charge. The consequence is an attractive interaction between the two electrons. The now correlated pair of electrons is referred to as a Cooper pair. Cooper pairs occupy a collective state and move through the crystal lattice unimpeded. The formation of Cooper pairs causes the observed (ex. Townsend and Sutton [10]) energy gap above the Fermi energy that was predicted by Frölich [11] in 1950. The electron-phonon interaction is suggested by the observation that the critical temperature depends on isotopic mass [12, 13].

The net momentum of Cooper pairs remains constant in the superconducting state, otherwise the Cooper pairs could not exist as a single coherent wavefunction that extends over the volume of the superconductor [14]. When sufficient energy is supplied to Cooper pairs, they will decouple and the superconducting state ceases. Since the momentum is proportional to current density, the energy required to break Cooper pairs implies the existence of a critical current density J_c [15]. When J_c is exceeded, the Cooper pairs are destroyed. The energy required to break Cooper pairs also comes in the form of thermal energy from the vibrations of the crystal lattice and magnetic energy from magnetic fields. The former implies the existence of a critical temperature T_c , mentioned above, while the latter suggests the existence of a critical magnetic field H_c . The critical field depends on material and is temperature-dependent according to the following equation [16], [17]:

$$H_c = H_0 \left[1 - \left(\frac{T}{T_c} \right)^2 \right], \quad (28)$$

where H_0 is the value of the critical field strength as $T \rightarrow 0$.

1.4 Type I and Type II Superconductors

Magnetic measurements on superconducting alloys and metals with impurities in the 1930's [18–20] showed different behavior in the superconducting state than those of pure metals. In particular, magnetic flux penetration occurred over a large range of applied magnetic fields while the material still showed zero electrical resistance. The experimental data were explained in a 1957 paper by A. A. Abrikosov [21]. There are two types of superconductors: Type I and Type II. Superconductors classified as Type I exhibit the Meissner effect and zero resistance below a critical field H_c and critical temperature T_c . Type II superconductors have two critical magnetic fields H_{c1} and H_{c2} . When a Type II material is cooled below the critical temperature T_c and subjected to a magnetic field $H_a < H_{c1}$, it exhibits no resistance and interior magnetic fields are completely expelled like a Type I superconductor. With $H_a > H_{c2}$, the material is no longer superconducting, again, like a Type I superconductor. For H_a between H_{c1} and H_{c2} , however, a Type II superconducting material is in a mixed state or vortex state where part of the material is penetrated by the field. Filaments of material are penetrated by quantized magnetic flux which are encircled by quantized supercurrents. In the vortex state the material still maintains zero resistance.

1.5 High-Temperature Superconductors

In 1986, J. G. Bednorz and K. A. Müller [22] reported that the metal oxide ceramic $\text{La}_{2-x}\text{Ba}_x\text{CuO}_4$ becomes superconducting above 30 K. Up to that point, the compound Nb_3Ge had the highest critical temperature of 23.2 K [23]. The superconductivity of $\text{La}_{2-x}\text{Ba}_x\text{CuO}_4$ initiated a flurry of research on a new family of materials referred to as high-temperature superconductors. M. K. Wu et al. [24] found that another copper oxide $\text{YBa}_2\text{Cu}_3\text{O}_7$ (YBCO) is superconducting with a critical tempera-

ture of 92 K. YBCO was the first superconductor found to have a critical temperature above the boiling point of nitrogen at 77 K. Many more copper-oxide, or cuprate, high-temperature superconductors were subsequently discovered including $\text{Bi}_2\text{Sr}_2\text{CaCu}_2\text{O}_8$ with $T_c \approx 105$ K [25], $\text{Tl}_2\text{Ba}_2\text{Ca}_2\text{Cu}_3\text{O}_{10}$ with $T_c \approx 120$ K [26], and $\text{HgBa}_2\text{Ca}_2\text{Cu}_3\text{O}_8$ with the highest critical temperature to date of $T_c \approx 134$ K [27]. The existence of many copper oxide superconductors is a consequence of the versatility of copper oxide in forming perovskite structured oxides when combined with alkaline earth, rare earth, and lone-pair ion oxides [28]. The general structure of cuprate superconductors consists of layers of CuO_2 separated by intermediary AO-type layers and MO_2 -type layers stacked in different sequences [28] with “A” representing alkaline earth metals and “M” representing a transition or other metals. Certain iron-based materials are also high-temperature superconductors. Iron-based superconductors contain layers of iron and elements from group 15 of the periodic table called pnictogens. Examples include the family $\text{ReFeAsO}_{1-\delta}$ ($\text{Re} = \text{Sm}, \text{Nd}, \text{Pr}, \text{Ce}, \text{La}$) with critical temperatures ranging from 26 K to 55 K [29]. All high-temperature superconductors known at the present time are classified as type II superconductors.

1.6 $\text{YBa}_2\text{Cu}_3\text{O}_{7-x}$

The crystal structure of $\text{YBa}_2\text{Cu}_3\text{O}_7$ (“Y123”) is characterized by the arrangement of copper-oxygen planes and copper-oxygen chains [31]. The stacking sequence of YBCO layers along the c -axis of the crystal goes as follows: $\text{CuO-BaO-CuO}_2\text{-Y-CuO}_2\text{-BaO}$ [32]. The perovskite structure layers of YBCO are separated by planes of CuO_2 with yttrium atoms between the copper-oxygen planes. The planes consist of a square lattice of copper atoms bridged by oxygen atoms [33]. Chains of CuO are parallel to the copper-oxygen planes with barium atoms located between the planes and chains. The unit cell of $\text{YBa}_2\text{Cu}_3\text{O}_7$ is shown in Figure 1.

Varying the oxygen content of $\text{YBa}_2\text{Cu}_3\text{O}_{7-x}$ results in significant changes of its physical properties. Many studies have shown that the critical temperature and crystal structure of $\text{YBa}_2\text{Cu}_3\text{O}_{7-x}$ change with oxygen content [31, 33, 34, 36–42]. Neutron diffraction and magnetic measurements have shown that T_c is dependent on the charge balance between the copper-oxygen chains and copper-oxygen planes [34]. The chain sites serve as charge reservoirs from which electrons are transferred to the copper-oxygen planes as the oxygen content decreases. It is within the copper-oxygen planes that superconductivity originates. As the oxygen content of $\text{YBa}_2\text{Cu}_3\text{O}_{7-x}$ decreases, so does T_c . The material goes through a structural change and the material’s superconductivity disappears when the oxygen content is below 6.3.

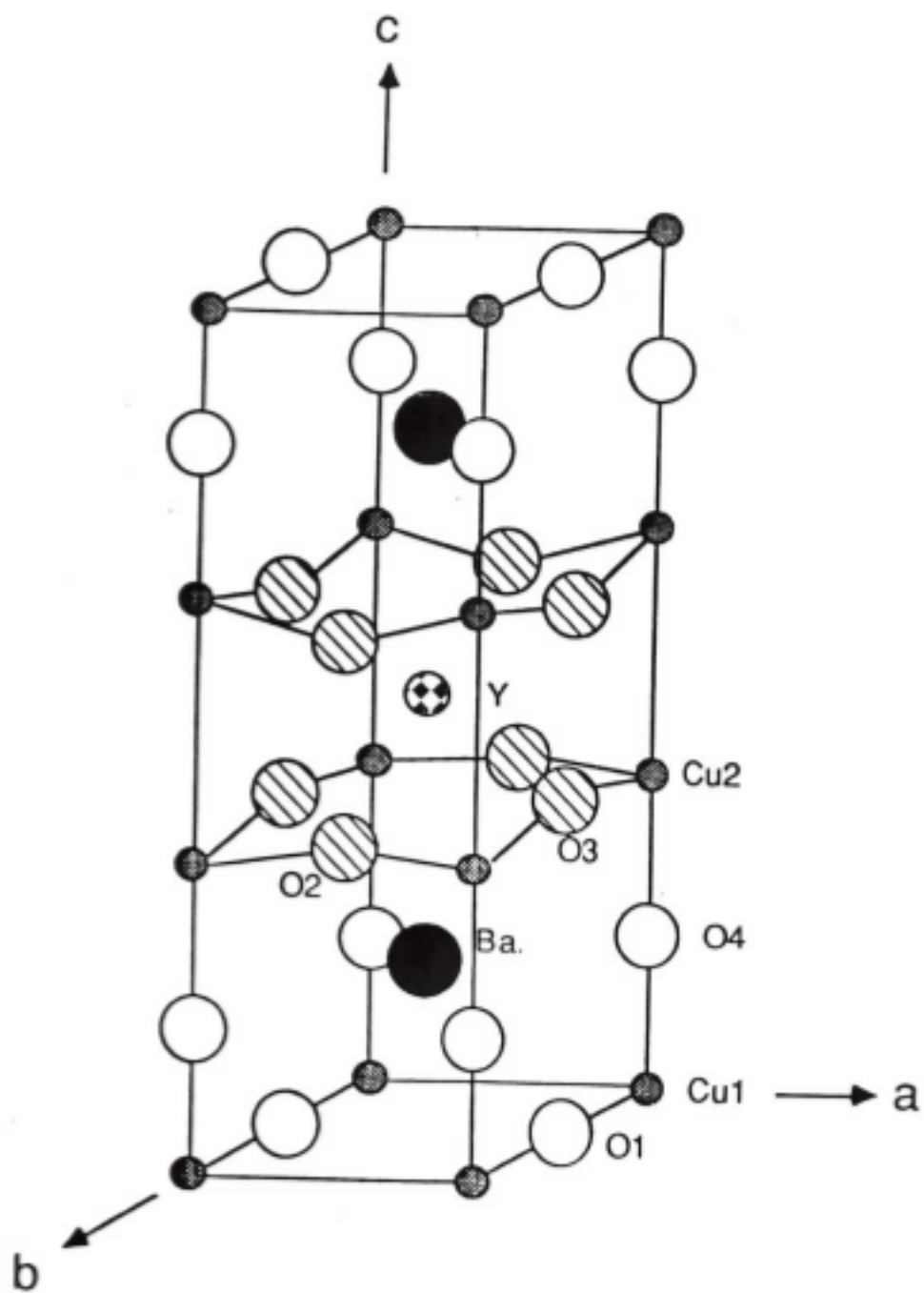


Figure 1: Crystal structure of $\text{YBa}_2\text{Cu}_3\text{O}_7$.

1.7 Crystal Structure

Solid matter exhibiting crystal structure consists of atoms or molecules arranged in a regular, repeating pattern in three dimensions. The crystal lattice is a mathematical construction of points in space that describes the periodic array of atoms in a crystal. The atom or group of atoms that forms this array is called the basis. The lattice is defined by lattice vectors \mathbf{a} , \mathbf{b} , and \mathbf{c} that are invariant under translation, that is to say for an observer located at a basis site, the crystal looks exactly the same from any other site. The parallelepiped that is formed by the lattice vectors is a minimum-volume cell called a unit cell [8]. The lengths of the lattice vectors are referred to as lattice constants a , b , and c and the angles formed by the lattice vectors are α , β , and γ . Figure 2 shows a crystal unit cell labeled with lattice constants and angles. Listed in Table 1 are the seven crystal systems in three dimensions along with each system's restrictions on unit cell lattice constants and angles. The orthorhombic system, for example, requires that $a \neq b \neq c$ and $\alpha = \beta = \gamma = 90^\circ$.

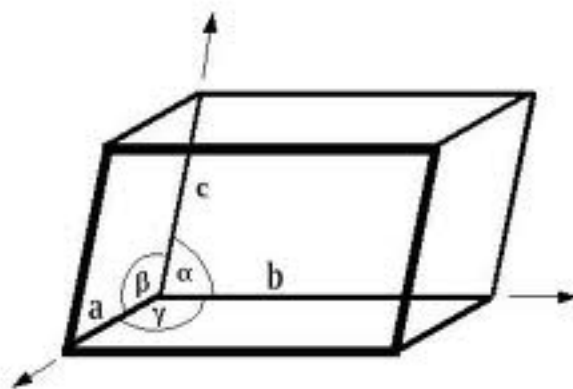


Figure 2: A crystal unit cell.

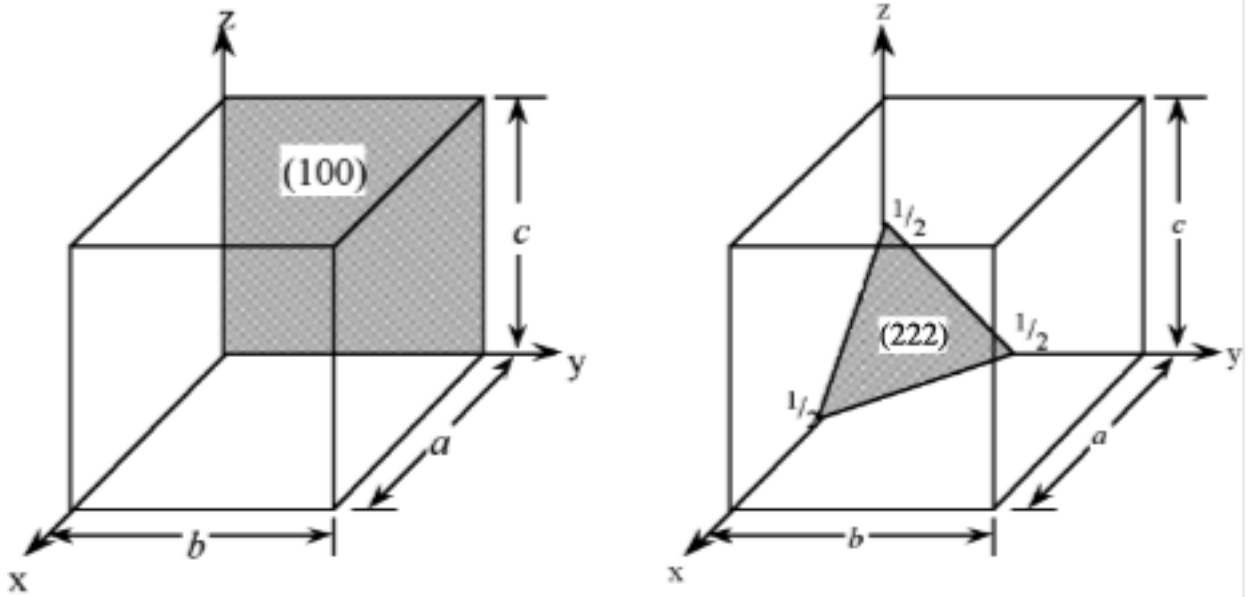
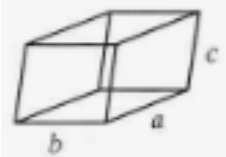
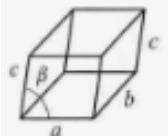
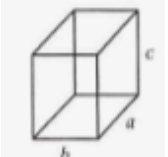
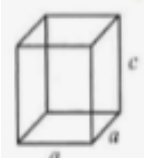
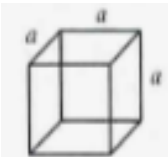
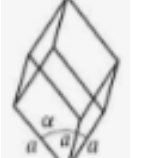
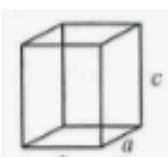


Figure 3: Illustration of the (100) and (222) crystal planes, indicated by shaded regions, and where they intersect the x -, y -, and z -axis.

Crystal planes are defined by three non-collinear points. The orientation of a set of crystal planes is characterized by Miller indices (hkl) . The h , k , and l indices are the reciprocal intercepts that a crystal plane makes with the crystallographic axes in a unit cell. Figure 3 gives two examples of crystal planes intercepting the crystal axes. The distance between crystal planes is d_{hkl} and can be expressed in terms of Miller indices and lattice constants. For example, d_{hkl} for orthrhombic structure is given by

$$d_{hkl} = \frac{1}{\sqrt{(h/a)^2 + (k/b)^2 + (l/c)^2}}. \quad (29)$$

Table 1: The seven crystal systems in three dimensions with restrictions on unit cell axial lengths and interaxial angles.

Crystal System	Unit cell axial length	Interaxial angles	Illustration
Triclinic	$a \neq b \neq c$	$\alpha \neq \beta \neq \gamma$	 A 3D diagram of a triclinic unit cell. The three axes are labeled a, b, and c, with a being the longest and c the shortest. The angles between the axes are not equal and not 90 degrees.
Monoclinic	$a \neq b \neq c$	$\alpha = \gamma = 90^\circ \neq \beta$	 A 3D diagram of a monoclinic unit cell. The axes are labeled a, b, and c. The angle between a and c is labeled beta, and it is shown to be different from 90 degrees. The angles between a and b, and b and c, are 90 degrees.
Orthorhombic	$a \neq b \neq c$	$\alpha = \beta = \gamma = 90^\circ$	 A 3D diagram of an orthorhombic unit cell. The axes are labeled a, b, and c. The cell is a rectangular prism where all three axes have different lengths, but all angles are 90 degrees.
Tetragonal	$a = b \neq c$	$\alpha = \beta = \gamma = 90^\circ$	 A 3D diagram of a tetragonal unit cell. The axes are labeled a, a, and c. The two base axes are equal in length, while the vertical axis is different. All angles are 90 degrees.
Cubic	$a = b = c$	$\alpha = \beta = \gamma = 90^\circ$	 A 3D diagram of a cubic unit cell. All three axes are labeled 'a', indicating they are all equal in length. All angles are 90 degrees.
Trigonal	$a = b = c$	$\alpha = \beta = \gamma < 120^\circ, \neq 90^\circ$	 A 3D diagram of a trigonal unit cell. The three axes are labeled 'a', 'a', and 'a', indicating they are all equal. The angle between two axes is labeled alpha, and it is shown to be less than 120 degrees and not 90 degrees.
Hexagonal	$a = b \neq c$	$\alpha = \beta = 90^\circ, \gamma = 120^\circ$	 A 3D diagram of a hexagonal unit cell. The axes are labeled a, a, and c. The two base axes are equal in length, while the vertical axis is different. The angle between the two base axes is 120 degrees, and the other two angles are 90 degrees.

1.8 X-ray Diffraction

X-ray wavelengths are comparable to the interplanar distances d_{hkl} of the crystalline solids. As a result, monochromatic X-rays incident upon crystalline matter are scattered by crystal planes. Constructive interference of diffracted X-ray beams occurs if the Bragg Law is satisfied:

$$n\lambda = 2d \sin \theta, \quad (30)$$

where n is an integer, λ is the X-ray wavelength, θ is the angle between the incident X-rays and the crystal plane, and d is the interplanar distance. By considering all orders of diffraction as first order diffraction, the Bragg Law can be rewritten as

$$\lambda = 2d \sin \theta. \quad (31)$$

The Bragg Law is illustrated in Figure 4. For a particular X-ray wavelength λ , when d -spacing of crystal planes and scattering angle θ satisfy the Bragg law, a peak of intensity will appear in the diffraction pattern. Diffraction peak positions are determined by the crystal symmetry and the lattice parameters of the crystal. The intensity of diffracted X-ray beams, however, is directly related to the position and number of electrons associated with each atom in the unit cell [44].

X-ray diffraction measurements can be produced from a fine powder of crystalline material. Since the powder consists of many randomly oriented crystal grains, each grain diffracts incident X-rays and generates diffraction peaks that correspond to specific sets of (hkl) crystal planes as the scattering angle 2θ is varied. The large number of grains and the random orientation of the grains assure that all (hkl) planes are observed as diffraction peaks.

A crystalline material produces a characteristic diffraction pattern depending on

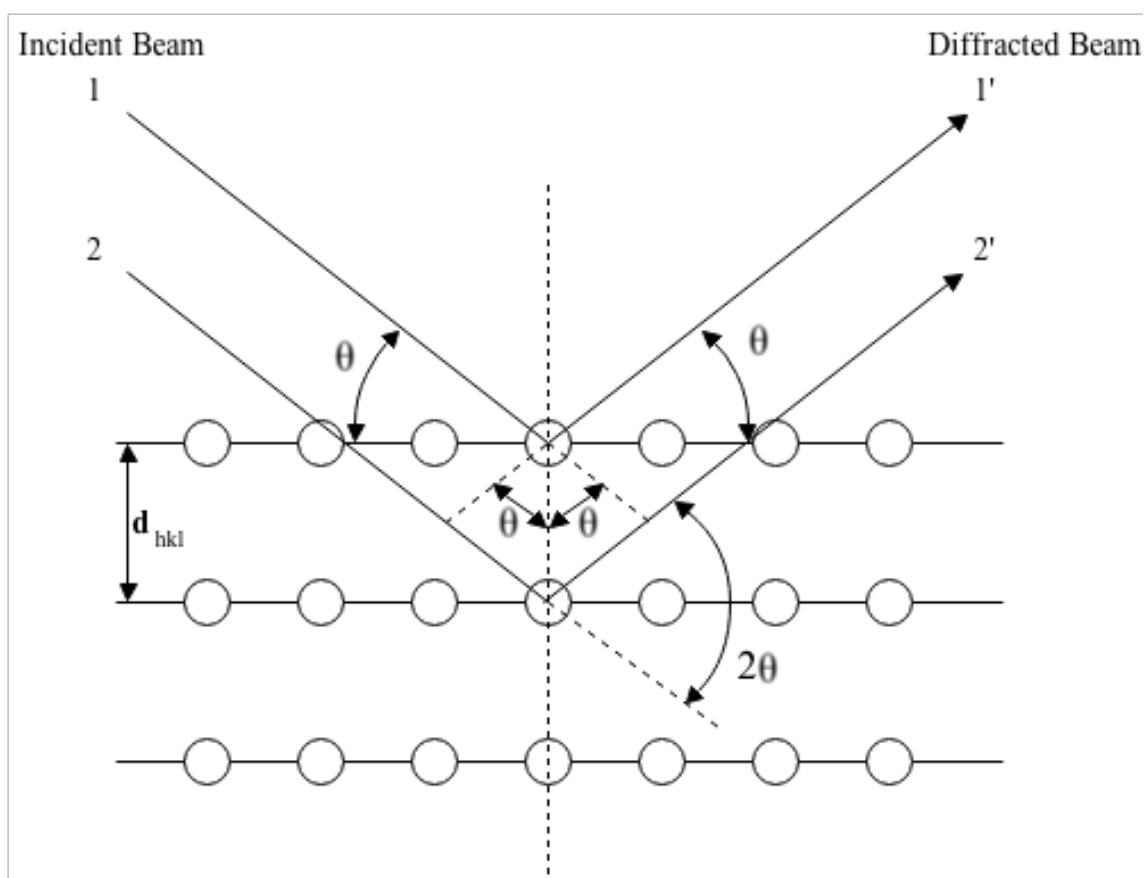


Figure 4: Diagram of the Bragg Law showing the relationship between the diffraction angle θ and the distance between crystal planes d_{hkl} .

the composition and crystal structures which are referred to as phases. From the diffraction data, the peak positions and relative intensities can be used to distinguish crystalline phases as well as determine the crystal structures. The lattice parameters of a crystalline phase can be calculated by using the Rietveld refinement method [43]. Rietveld refinement is a least squares fit method that attempts to fit the experimental powder diffraction data with a diffraction pattern calculated from the composition and crystal structure of a compound.

2 Experimental Procedures

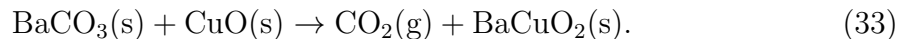
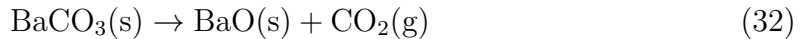
2.1 Sample Synthesis

Oxygen deficient samples used in this study were created from a single batch of $\text{YBa}_2\text{Cu}_3\text{O}_7$. Starting materials were ground, mixed and subjected to several heat treatments that facilitate the necessary chemical reactions for the creation of the final single-phase product. Long annealing time was necessary to produce fully oxygenated sample. It was crucial to repeatedly grind the sample to promote homogeneity of the constituent compounds so that chemical reactions proceed in a uniform manner [7]. To prevent contamination, care has been taken to make sure all instruments used in the sample synthesis were cleaned thoroughly.

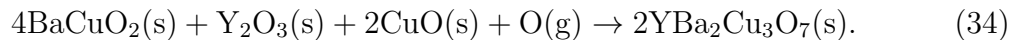
2.1.1 The Original Sample

Starting materials consisted of yttrium oxide (Y_2O_3), barium carbonate (BaCO_3), and copper oxide (CuO). Yttrium oxide was dried by heating the powder in a box furnace at 800°C for 40 hours and then cooled before it was stored in a desiccator. Copper oxide was heated at 820°C in a tube furnace for 56 hours in oxygen atmosphere to ensure complete oxygenation. The powders were combined in stoichiometric ratio to form a 12g mixture and ground in an agate mortar with a pestle for 50 minutes. After pouring the mixture into a clean die, a hydraulic press was used to press the mixture to a pellet under an approximate pressure of 8000-psi. The pellet was placed on an alumina (Al_2O_3) plate and put in an alumina crucible. The sample was calcined in air at 900°C for 24 hours three times with intermediate grindings. The final heat treatment was done in a tube furnace in flowing oxygen with a flow rate of ≈ 15 cc/min. The sample was sintered at 965°C for 40 hours, then annealed at 665°C for 8 hours and 400°C for 24 hours before cooled to room temperature.

The initial heat treatments facilitate three essential chemical reactions. Two reactions take place in the process of calcination: 1) solid (s) BaCO_3 decomposes into solid BaO and gaseous (g) CO_2 and 2) solid BaCO_3 reacts with solid CuO to form gaseous CO_2 and solid BaCuO_2 [7]:



In the process of sintering, adjacent particles in a powder mixture react and bond [7]. In the final chemical reaction, BaCuO_2 reacts with Y_2O_3 and CuO to form $\text{YBa}_2\text{Cu}_3\text{O}_7$ and gaseous oxygen:



Annealing in oxygen serves to fully oxygenate the sample and stabilize the crystal structure.

2.1.2 The Oxygen-Deficient Samples

Oxygen deficient samples $\text{YBa}_2\text{Cu}_3\text{O}_{7-x}$ (where $0 < x < 1$) were made by annealing small pieces removed from the fully-oxygenated sample (BH-5-YBCO) in air at temperatures ranging from 575°C to 780°C . After the annealing period, the sample was quenched in liquid nitrogen and stored in a desiccator for at least 12 hours to remove moisture that may have condensed on the sample's surface. The change in mass was measured to determine the final oxygen content of the samples. It was assumed that all of the loss in mass is entirely due to change in oxygen content from the initial stoichiometric value of 7.00. The initial number of moles for the sample, N_i , is the

same as the number of moles in every oxygen deficient sample, N_f :

$$N_i = N_f = N \quad (35)$$

The molar mass of $\text{YBa}_2\text{Cu}_3\text{O}_7$, $M(\text{Y123})$, is

$$M(\text{Y123}) = M(\text{Y}) + 2M(\text{Ba}) + 3M(\text{Cu}) + 7M(\text{O}), \quad (36)$$

where $M(\text{Y})$, $M(\text{Ba})$, $M(\text{Cu})$, and $M(\text{O})$ are the molar masses of yttrium, barium, copper, and oxygen, respectively. The molar mass of the oxygen deficient samples, $M(\text{YBCO})$, with x fewer oxygen atoms per mole is

$$M(\text{YBCO}) = M(\text{Y}) + 2M(\text{Ba}) + 3M(\text{Cu}) + (7 - x)M(\text{O}). \quad (37)$$

The mass of a sample is just the number of moles of the sample multiplied by the molar mass of the compound in the sample. Therefore, the initial mass of the sample, m_i , is

$$m_i = N_i [M(\text{Y}) + 2M(\text{Ba}) + 3M(\text{Cu}) + 7M(\text{O})]. \quad (38)$$

After the high-temperature anneal, the final mass, m_f , of the oxygen-deficient sample is

$$m_f = N_f [M(\text{Y}) + 2M(\text{Ba}) + 3M(\text{Cu}) + (7 - x)M(\text{O})]. \quad (39)$$

Using the fact that $N_i = N_f = N$, the change in mass $m_i - m_f = \Delta m$ is

$$\Delta m = xNM(\text{O}). \quad (40)$$

Solving for the oxygen loss, x , in Equation (40), we have

$$x = \frac{\Delta m}{NM(\text{O})}. \quad (41)$$

The uncertainty in oxygen content of the oxygen deficient samples follows from the variance formula:

$$\delta x = \sqrt{\left(\frac{\partial x}{\partial \Delta m}\right)^2 (\delta(\Delta m))^2 + \left(\frac{\partial x}{\partial N}\right)^2 (\delta N)^2}, \quad (42)$$

where δx , $\delta(\Delta m)$, and δN are the uncertainty in oxygen loss, change in mass, and number of moles, respectively. We assume there is no uncertainty in $M(\text{O})$. Since

$$N = \frac{m_i}{M(\text{Y123})}, \quad (43)$$

the uncertainty in the number of moles is

$$\delta N = \frac{\delta m_i}{M(\text{Y123})} = \frac{\delta m_i}{m_i} N. \quad (44)$$

The last step in (44) comes from the fact that $M(\text{Y123}) = m_i/N$. Then, the two partial derivative terms inside the radical of (42) can be rewritten as

$$\frac{\partial x}{\partial \Delta m} = \frac{1}{NM(\text{O})}, \quad (45)$$

and

$$\frac{\partial x}{\partial N} = -\frac{\Delta m M(\text{O})}{(NM(\text{O}))^2}. \quad (46)$$

The square of the uncertainty in the change in mass is

$$(\delta(\Delta m))^2 = (\delta m_i)^2 + (\delta m_f)^2. \quad (47)$$

Using the results of (44) through (47), equation (42) can be rewritten as

$$\begin{aligned} \delta x &= \sqrt{\left(\frac{1}{NM(\text{O})}\right)^2 [(\delta m_i)^2 + (\delta m_f)^2] + \left[-\frac{\Delta m M(\text{O})}{(NM(\text{O}))^2}\right]^2 \left(\frac{\delta m_i}{m_i} N\right)^2} \\ &= \frac{1}{NM(\text{O})} \sqrt{(\delta m_i)^2 + (\delta m_f)^2 + \left(\frac{\Delta m}{m_i}\right)^2 (\delta m_i)^2}. \end{aligned} \quad (48)$$

The term $\Delta m/m_i \sim 10^{-2}$, which means $(\Delta m/m_i)^2(\delta m_i)^2 \ll (\delta m_i)^2 + (\delta m_f)^2$. Therefore, the uncertainty in oxygen content is

$$\delta x \approx \frac{1}{NM(\text{O})} \sqrt{(\delta m_i)^2 + (\delta m_f)^2}. \quad (49)$$

The uncertainty in sample mass measurements was designated as

$\delta m_i = \delta m_f = \delta m = 0.2$ mg though the scales used for these measurements are sensitive to 0.1 mg. This was done to account for observed fluctuations in the digital readout of the scale during measurements. Therefore,

$$\delta x \approx \frac{\sqrt{2}\delta m}{NM(\text{O})}. \quad (50)$$

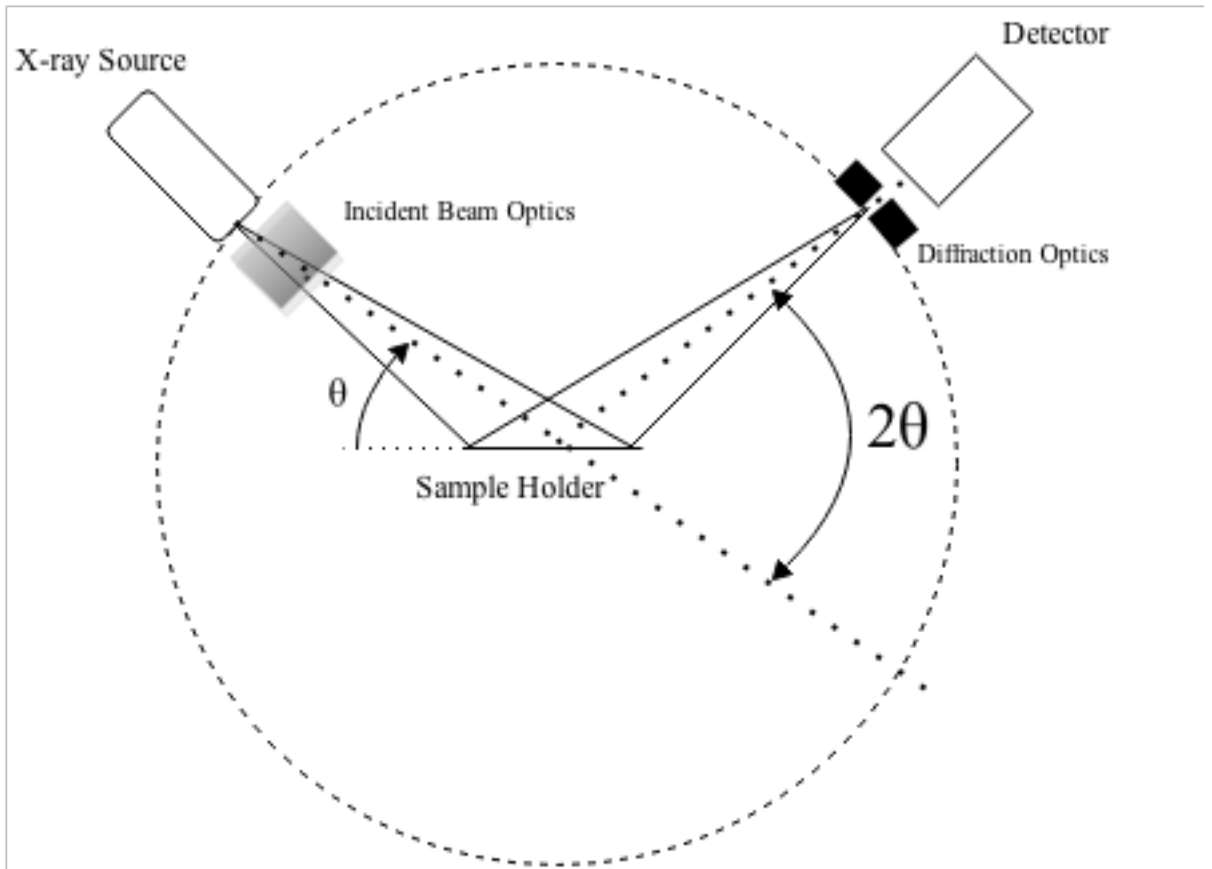


Figure 5: Schematic of X-ray diffractometer utilizing Bragg-Brentano geometry.

2.2 X-ray Diffraction

X-ray diffraction was conducted using a Rigaku Ultima IV X-ray diffractometer. Figure 2.2 illustrates the configuration of this diffractometer. Approximately 50 mg to 100 mg of YBCO sample was sprinkled on a Vaseline-greased glass slide. Silicon powder was used as an internal standard. Measurements of X-ray intensity versus scattering angle, 2θ , were executed with Cu $K\alpha$ radiation ($\lambda = 1.5406\text{\AA}$) between angles $20^\circ < 2\theta < 60^\circ$. The D/teX Ultra X-ray detector was used while the samples were scanned at a rate of $2.0^\circ/\text{min}$ while sampling at every 0.02° .

To ensure our samples did not contain unwanted phases, the diraction patterns

were indexed by comparing peak positions and intensities with the diffraction patterns from the International Center for Diffraction Data (ICDD) database. Lattice parameters were determined from the diffraction patterns using Rietveld structure refinement method [43] which comes with Rigaku PDXL software. Cell parameters and atom positions of $\text{YBa}_2\text{Cu}_3\text{O}_7$ from a calculated pattern were put in as a starting point for refinement. For each sample, the silicon phase peak profile was refined first and then set as the internal standard. Subsequent refinements only permitted certain refining parameter settings for YBCO and not silicon. For each YBCO refinement, the following refining parameters were selected: lattice constant, profile, crystal structure, temperature factor, and peak shift under the axial displacement model. Since previous research [34], [37] indicates that only one atom site in the YBCO crystal varies significantly in occupancy, the only atom occupancy that was allowed to refine was the O(4) site located along CuO chain (labeling of site follows from [32]). Refinements were considered acceptable upon reaching a goodness of fit value of $S \lesssim 2$. The goodness of fit value is the ratio of the residual whole pattern (Rwp) to minimum residual whole pattern (Re).

The diffraction patterns for each sample were indexed by comparing peak positions and intensities with the diffraction patterns from the ICDD.

2.3 Magnetic Measurements

Magnetic moment as a function of temperature was measured to determine the superconducting transition temperature of the sample. The measurements were done at Ames Laboratory, Iowa State University using a Quantum Design MPMS-5S SQUID (Superconducting QUantum Interface Device) magnetometer. SQUID magnetometers use DC Josephson effect to measure sample magnetic moments, and is sensitive

to 10^{-11} Am². A user-defined sequence can precisely control the temperature and the magnetic field in the instrument's superconducting solenoid. Magnetic fields from 0 T to 5 T can be generated and temperatures ranged from 2 K to 400 K for magnetic moment measurements.

Magnetic moment as a function of applied field and temperature was measured under two controlled sequences: zero field-cooled (ZFC) and field-cooled (FC). In the ZFC sequence, most samples were cooled to 10 K or 20 K with zero applied field. The magnetic moment was first measured at 10 K or 20 K as the field increased from 0 Oe to 20 Oe. The magnetic moment was then measured in a field of 20 Oe as the temperature increased to 100 K. For the FC sequence, the field remained at 20 Oe as the temperature decreased from 100 K to 20 K or 10 K.

3 Results

3.1 Samples Synthesized

The box furnace conditions for each oxygen-deficient sample and the resulting oxygen content are summarized in Table 2. Four samples were made to show that the procedure for creating oxygen-deficient YBCO produces samples with consistent oxygen compositions. Samples BH-5-YBCO-5 and BH-5-YBCO-7 were annealed at 750 °C in air to produce samples with oxygen content 6.44 ± 0.03 and 6.41 ± 0.02 , respectively. Samples BH-5-YBCO-4 and BH-5-YBCO-6 were annealed at 780 °C in air to produce samples with oxygen content 6.37 ± 0.02 and 6.33 ± 0.02 , respectively. Samples with oxygen content less than 6.60 were annealed for 20 hours, while samples with oxygen content more than 6.60 were annealed for 10 hours.

Table 2: Summary of box furnace settings for production of oxygen deficient samples $\text{YBa}_2\text{Cu}_3\text{O}_{7-x}$.

Sample Name	Oxygen Content	Box Furnace Temperature (°C)	Time (hours)
BH-5-YBCO	7.00 ± 0.03	-	-
BH-5-YBCO-14	6.79 ± 0.03	575	10
BH-5-YBCO-13a	6.73 ± 0.04	600	10
BH-5-YBCO-15	6.65 ± 0.02	625	10
BH-5-YBCO-2	6.54 ± 0.02	675	20
BH-5-YBCO-8	6.46 ± 0.02	720	20
BH-5-YBCO-5	6.44 ± 0.03	750	20
BH-5-YBCO-7	6.41 ± 0.02	750	20
BH-5-YBCO-4	6.37 ± 0.02	780	20
BH-5-YBCO-6	6.33 ± 0.02	780	20

3.2 Crystal Structure

X-ray diffraction patterns for each YBCO sample along with labeled silicon peaks are presented in Figures 6 - 11. All of the peaks in each diffraction pattern are indexable to $\text{YBa}_2\text{Cu}_3\text{O}_{7-x}$ phase. This indicates all samples are single phased. Small shifts in diffraction peak positions are observed as the oxygen content is changed. Table 3 summarizes the lattice parameters for six YBCO samples with oxygen contents ranging from 7.00 to 6.33. The data reveal that as the oxygen is removed, a and c increase while b decreases monotonically except for the sample with oxygen content of 6.79. The unit cell volume is observed to increase as the oxygen content decreases. The volume appears to decrease slightly before it starts to increase at oxygen content of 6.54. Plots of lattice parameters as a function of oxygen content $7 - x$ are shown in Figure 12. Unit cell volume versus oxygen content is shown in Figure 13.

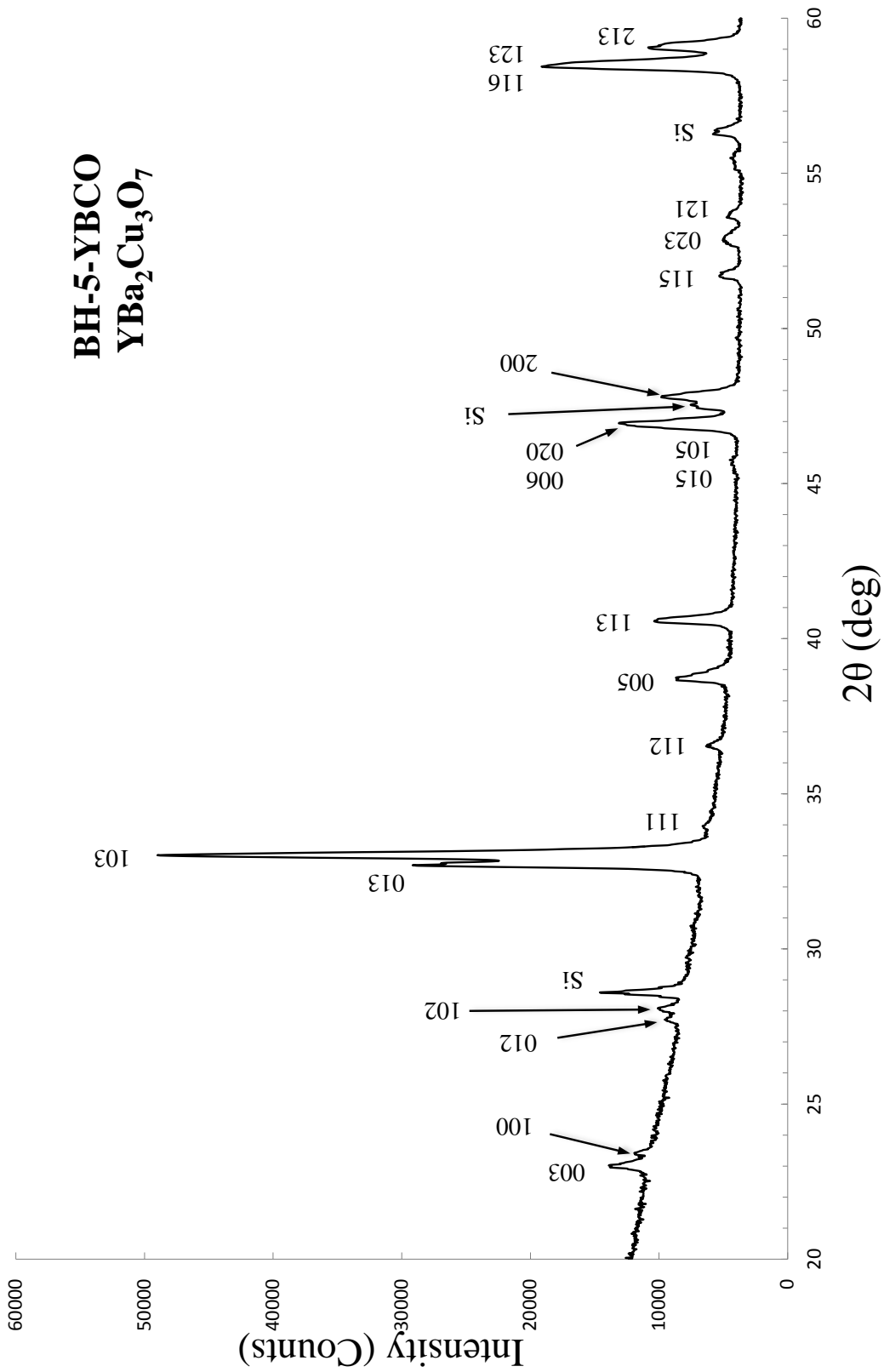


Figure 6: X-ray Diffraction pattern with indexed peaks of sample BH-5-YBCO with composition YBa₂Cu₃O₇. Silicon standard peaks are also labeled.

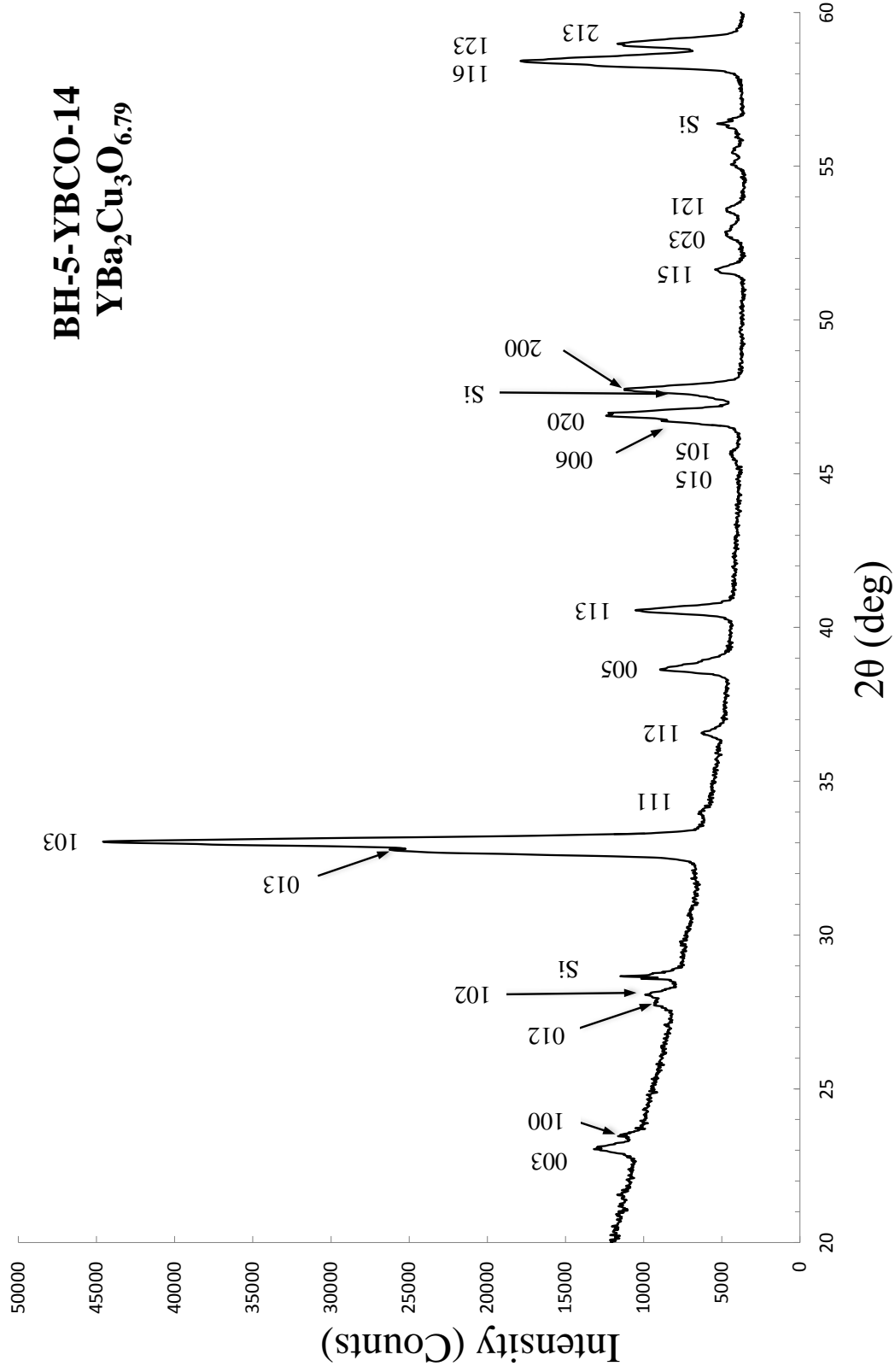


Figure 7: X-ray Diffraction pattern with indexed peaks of sample BH-5-YBCO-14 with composition YBa₂Cu₃O_{6.79}. Silicon standard peaks are also labeled.

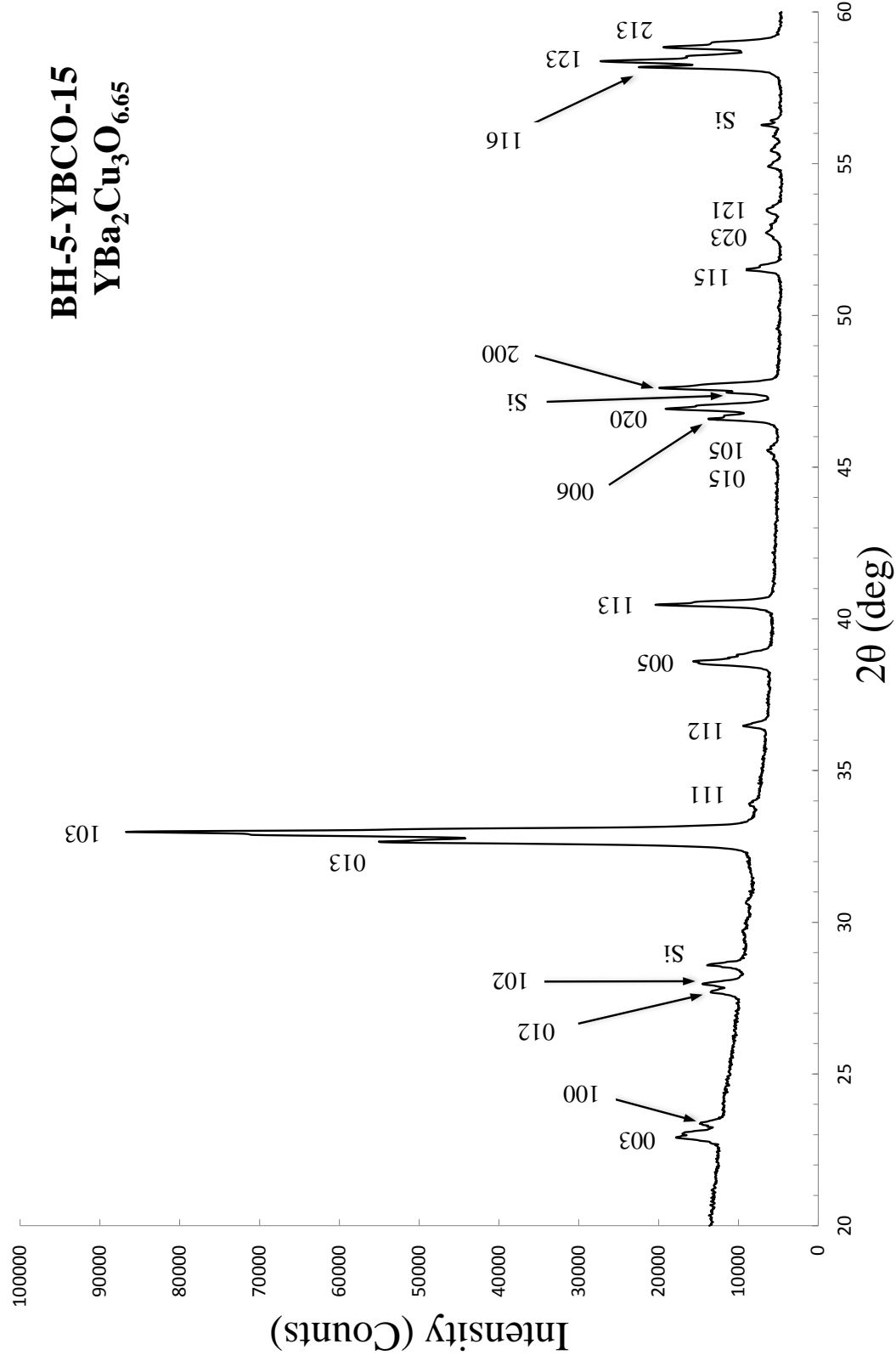


Figure 8: X-ray Diffraction pattern with indexed peaks of sample BH-5-YBCO-15 with composition YBa₂Cu₃O_{6.65}. Silicon standard peaks are also labeled.

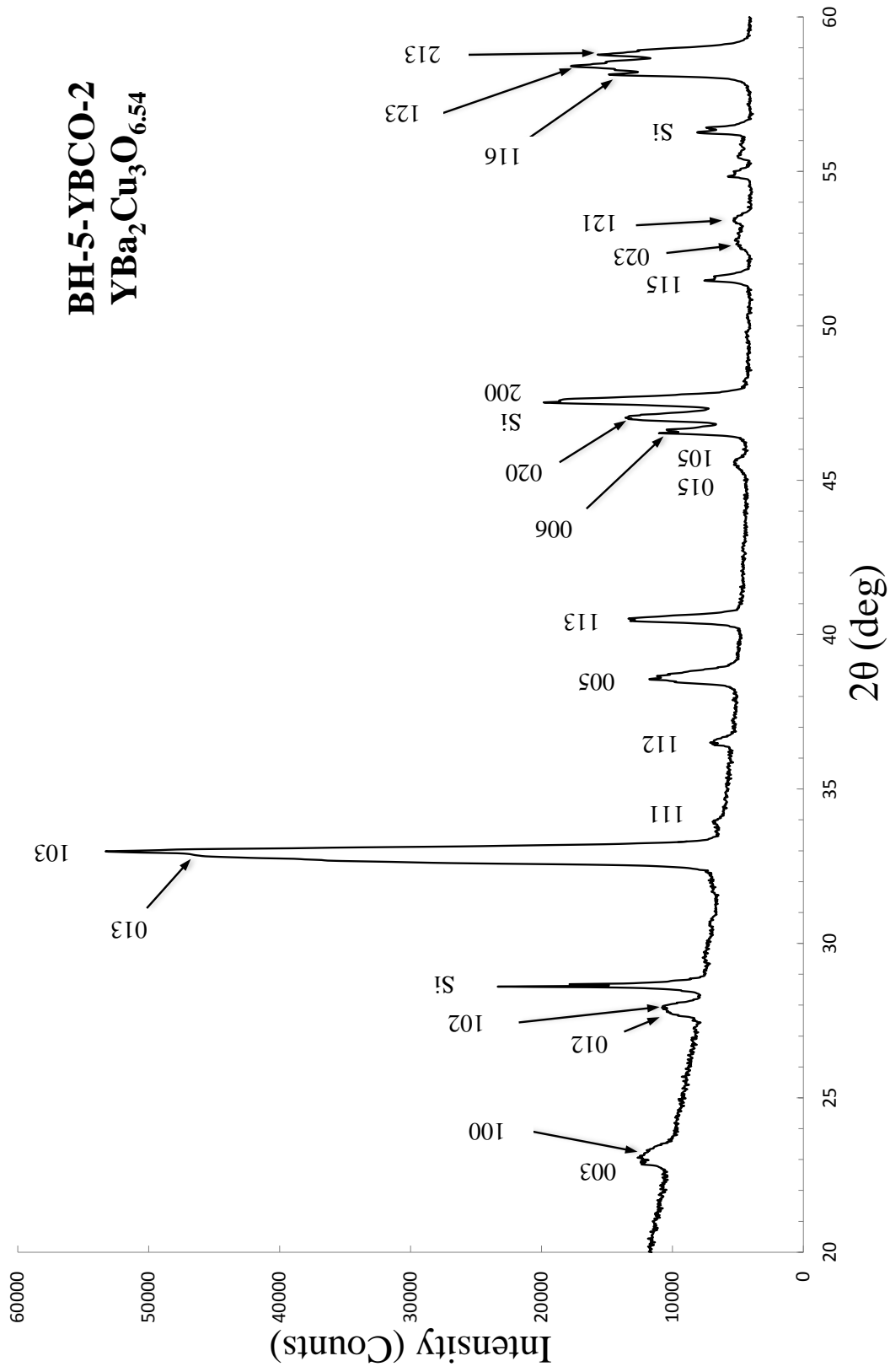


Figure 9: X-ray Diffraction pattern with indexed peaks of sample BH-5-YBCO-2 with composition YBa₂Cu₃O_{6.54}. Silicon standard peaks are also labeled.

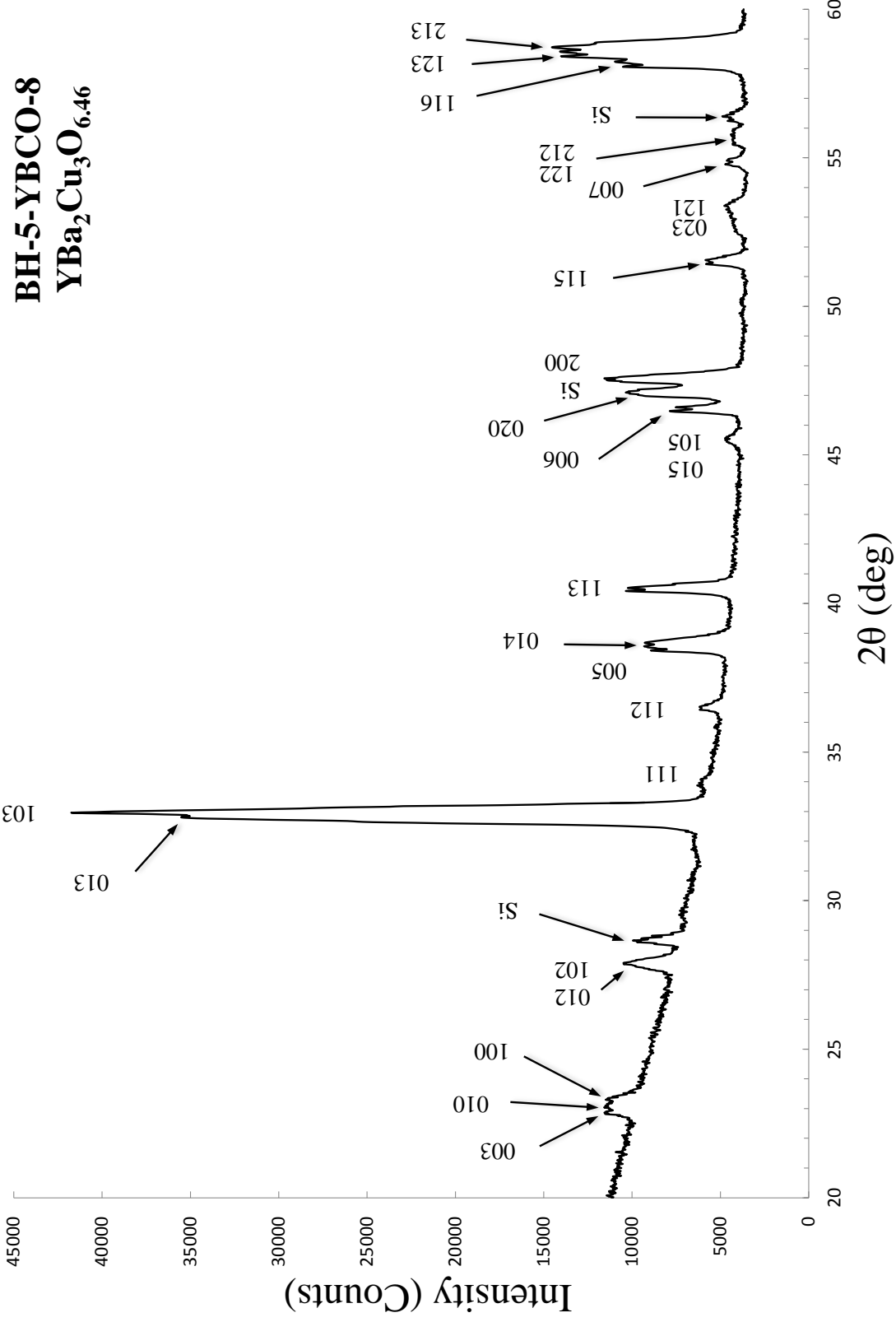


Figure 10: X-ray Diffraction pattern with indexed peaks of sample BH-5-YBCO-8 with composition YBa₂Cu₃O_{6.46}. Silicon standard peaks are also labeled.

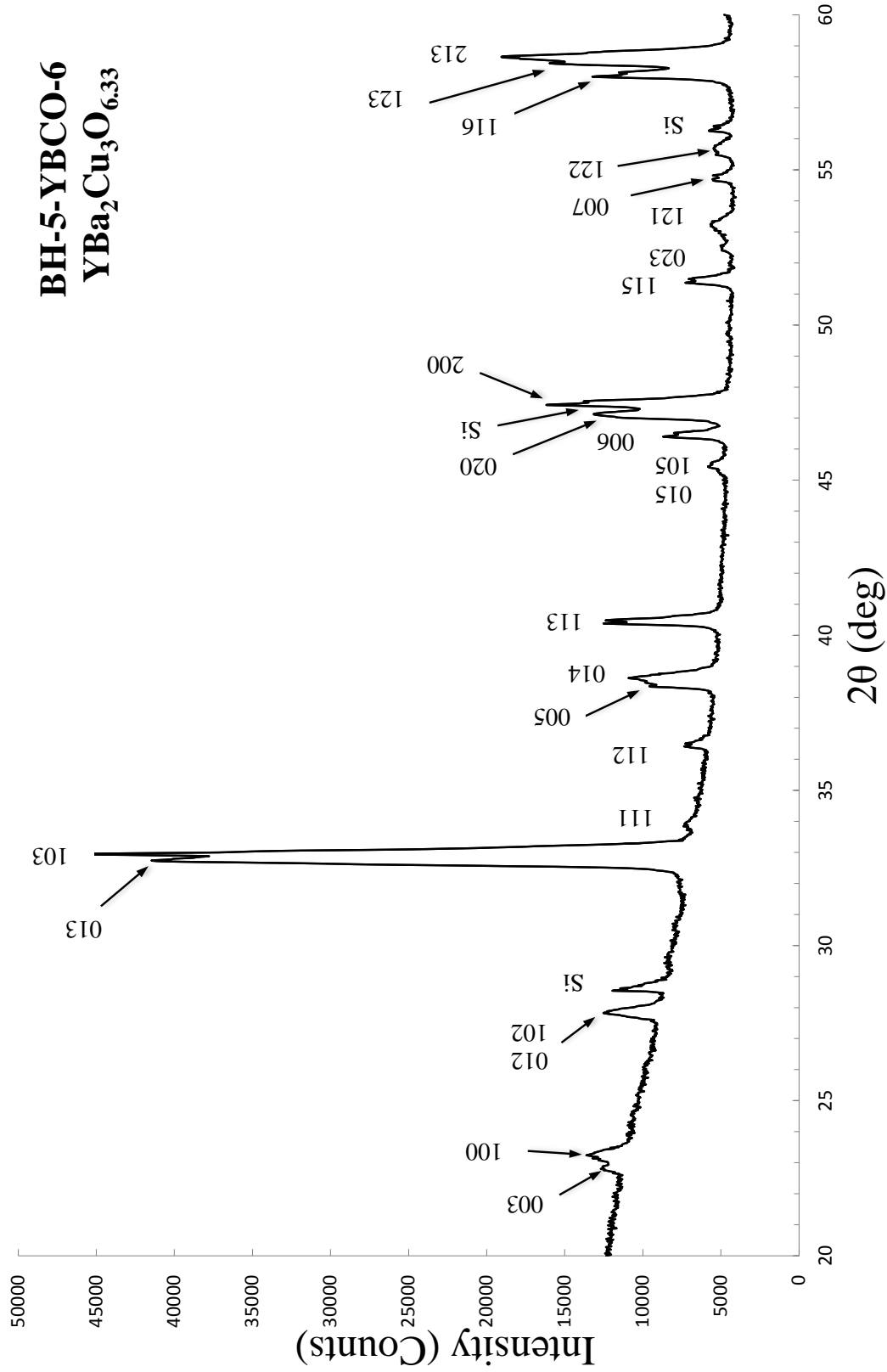


Figure 11: X-ray Diffraction pattern with indexed peaks of sample BH-5-YBCO-6 with composition YBa₂Cu₃O_{6.33}. Silicon standard peaks are also labeled.

Table 3: Lattice parameters and unit cell volume for oxygen-deficient samples of $\text{YBa}_2\text{Cu}_3\text{O}_{7-x}$. Numbers in parentheses give the standard deviations of the last significant digit.

Sample Composition	a (Å)	b (Å)	c (Å)	Volume (Å ³)
$\text{YBa}_2\text{Cu}_3\text{O}_7$	3.8154(1)	3.8811(2)	11.6701(4)	172.8093(5)
$\text{YBa}_2\text{Cu}_3\text{O}_{6.79}$	3.8252(1)	3.8871(2)	11.7162(8)	174.2070(8)
$\text{YBa}_2\text{Cu}_3\text{O}_{6.65}$	3.8285(2)	3.8804(2)	11.7216(5)	174.1338(6)
$\text{YBa}_2\text{Cu}_3\text{O}_{6.54}$	3.8323(2)	3.8746(1)	11.7311(4)	174.1917(5)
$\text{YBa}_2\text{Cu}_3\text{O}_{6.46}$	3.8357(4)	3.8722(3)	11.746(1)	174.457(1)
$\text{YBa}_2\text{Cu}_3\text{O}_{6.33}$	3.8396(2)	3.8678(1)	11.7576(4)	174.6089(5)

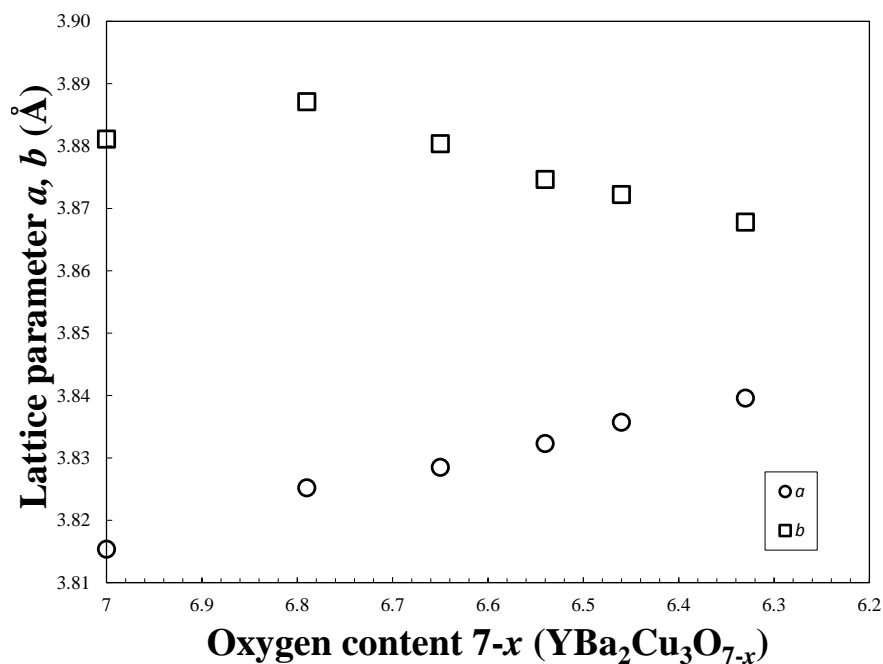
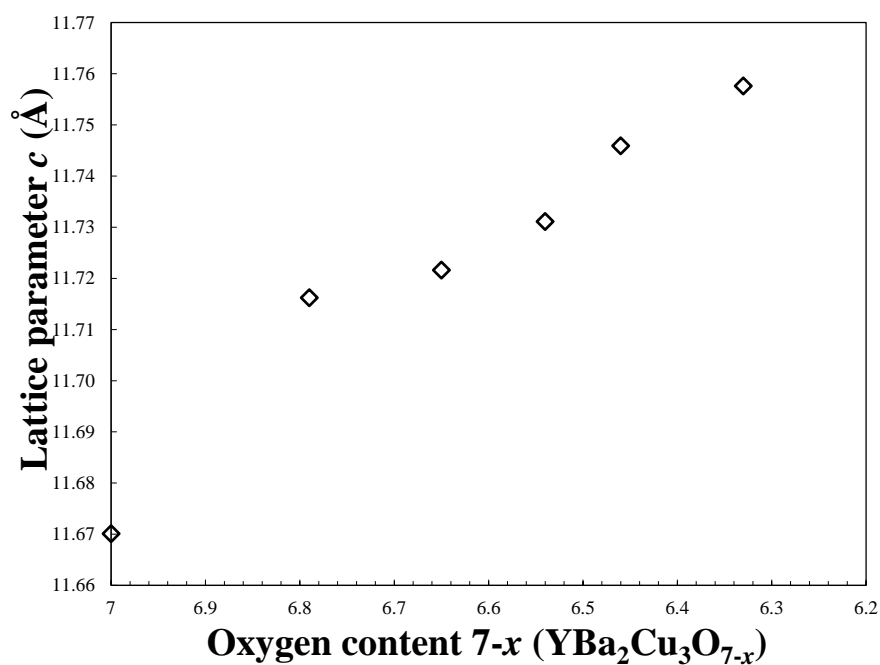
(a) Lattice parameters a and b versus oxygen composition $7 - x$.(b) Lattice parameter c versus oxygen composition $7 - x$.

Figure 12: Lattice parameters (a) a and b , and (b) c of $\text{YBa}_2\text{Cu}_3\text{O}_{7-x}$ as a function of oxygen composition $7-x$. Lattice parameters were determined by Rietveld refinement of X-ray diffraction data while the oxygen compositions were determined from mass-loss measurements of quenched samples. Error bars are smaller than the size of the symbols.

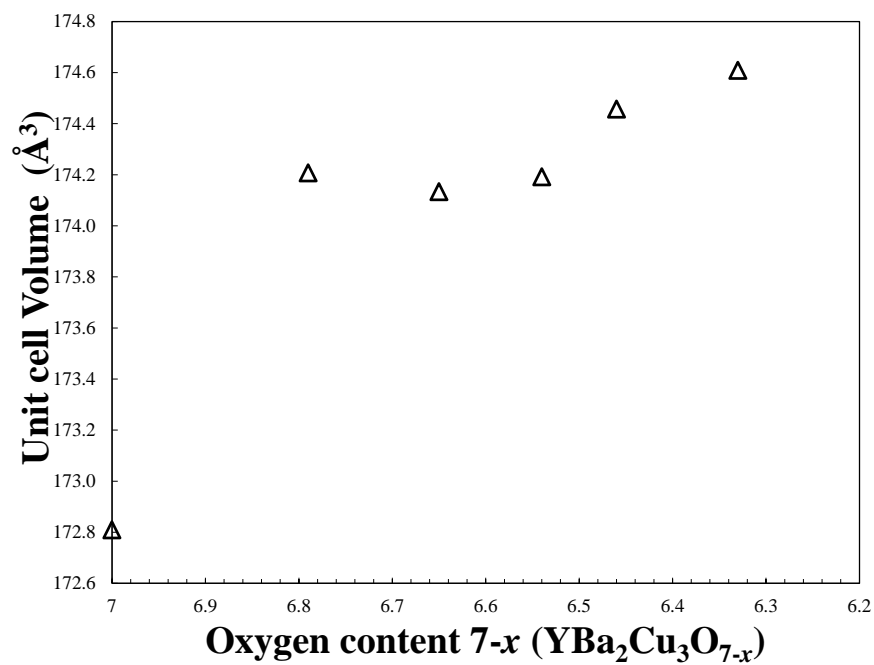


Figure 13: Unit cell volume, V , versus oxygen composition $7 - x$. Error bars are smaller than the size of the symbols.

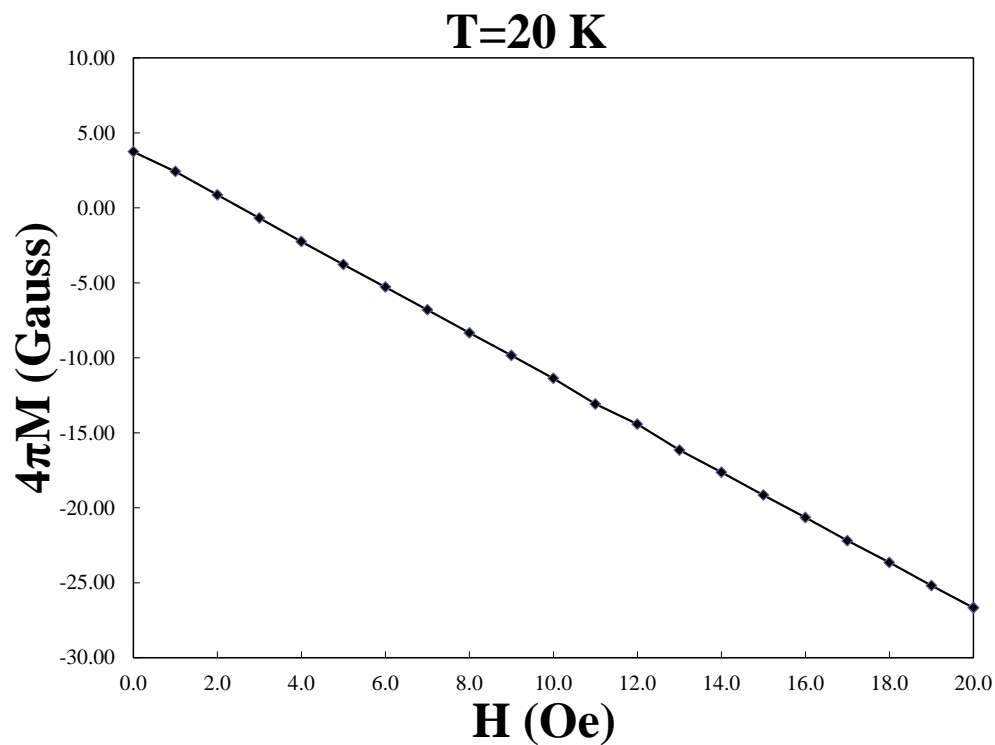
3.3 Superconducting Transition Temperature

Magnetic moment measurements for oxygen-deficient samples are presented in Figures 14-19. The top graph in each figure shows the magnetic moment measured as a function of applied field H . In the bottom graph of each figure, mass magnetization, M , as a function of temperature is shown. Shown in magnetic moment versus temperature plots are zero-field cooled (ZFC) curve, which measures the Meissner signal, and field-cooled (FC) curve, which measures the shielding effect.

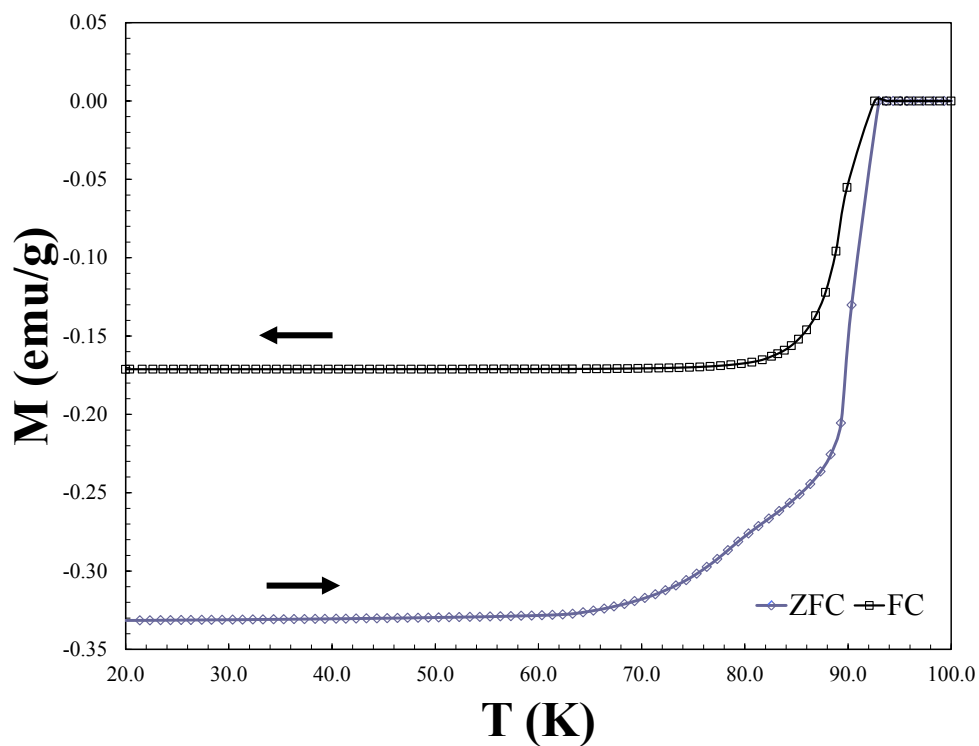
A diamagnetic signal is observed for all samples when magnetization is plotted as a function of applied field. However, only the sample with oxygen content of 6.79 in Figure 15(a) shows a near perfect diamagnetic signal of $\chi = -1$. For the fully-oxygenated sample in Figure 14(a), $\chi < -1$. The remaining samples have $-1 < \chi < 0$. Meissner signal decreases (becomes less negative) with decreasing oxygen content. The sample with oxygen content of 6.33 shown in Figure 19(a) exhibits the weakest diamagnetic signal.

For each sample, the superconducting transition temperature is taken as the midpoint temperature between 10% and 90% of the superconducting transition. The transition width of a sample's T_c is the temperature range 50% to 90% and 50% to 10% of the superconducting transition. For the sample with oxygen content of 6.33, the superconducting transition is not complete. The superconducting transition temperature for this sample is estimated using the point where the line tangent to the region of steepest descent on the FC curve intersects the normal state magnetization. The superconducting transition temperatures are listed in Table 4. Also listed in Table 4 are the fractions of superconductor in each sample. The fraction is the value of magnetic susceptibility in the field-cooled measurement when the transition is complete. The data reveal that superconducting transition temperatures and

superconducting fraction of the samples decrease with oxygen content. Transition temperature is plotted as a function of oxygen content, $7 - x$, in Figure 20. The transition temperature is observed to drop steeply from 85.6 K for the fully-oxygenated sample to 57.6 K for the sample with oxygen content of 6.79. Transition temperatures then appear to gradually decrease before dropping sharply to less than 14.5 K for the sample with oxygen content of 6.33. The superconducting fraction is highest in the fully oxygenated sample (68%) and decreases as the oxygen content decreases. The superconducting fraction cannot be accurately determined for BH-5-YBCO-6 as a result of incomplete transition from the non-superconducting state.

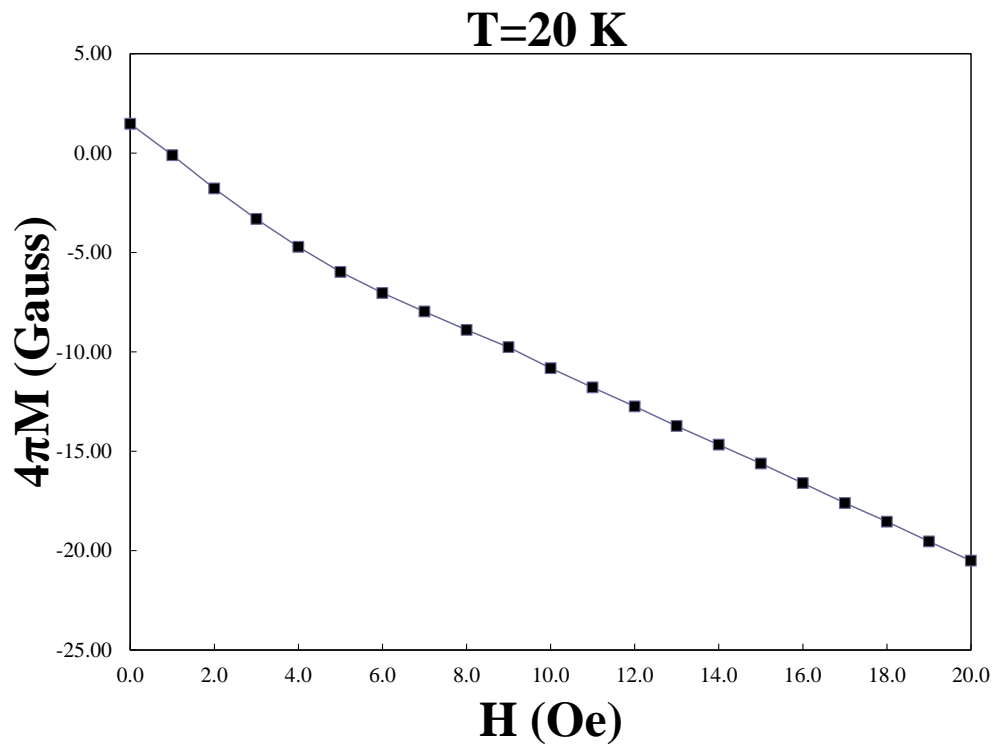


(a) Volume magnetic moment, M , versus applied magnetic field strength, H .

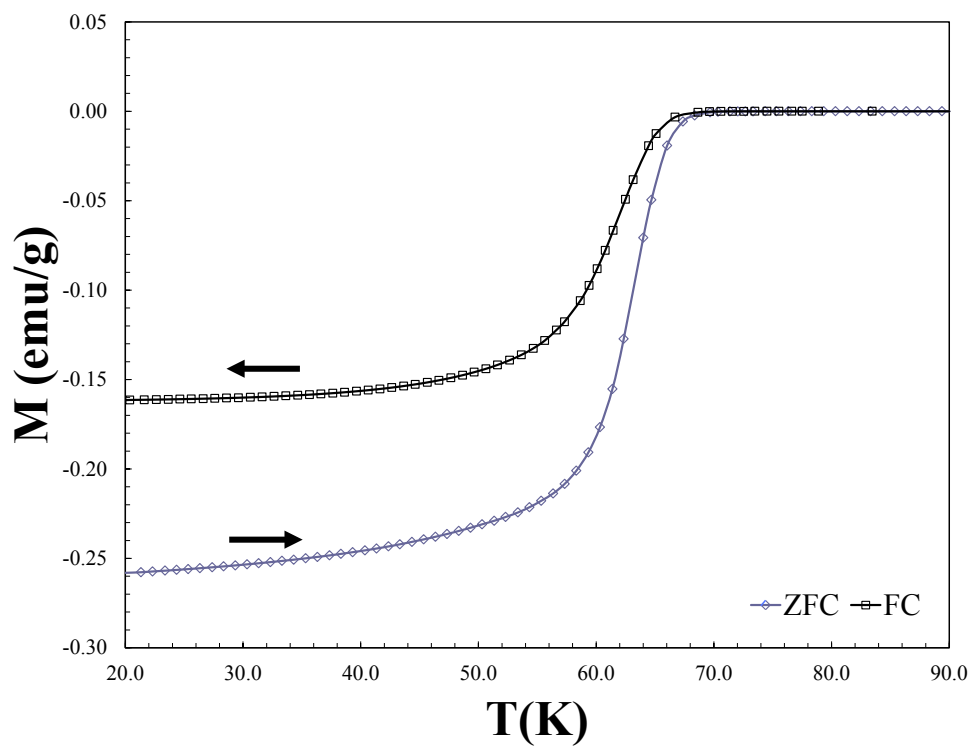


(b) Magnetic moment, M , versus temperature, H .

Figure 14: Magnetic moment measurements for sample BH-5-YBCO with composition $\text{YBa}_2\text{Cu}_3\text{O}_7$.

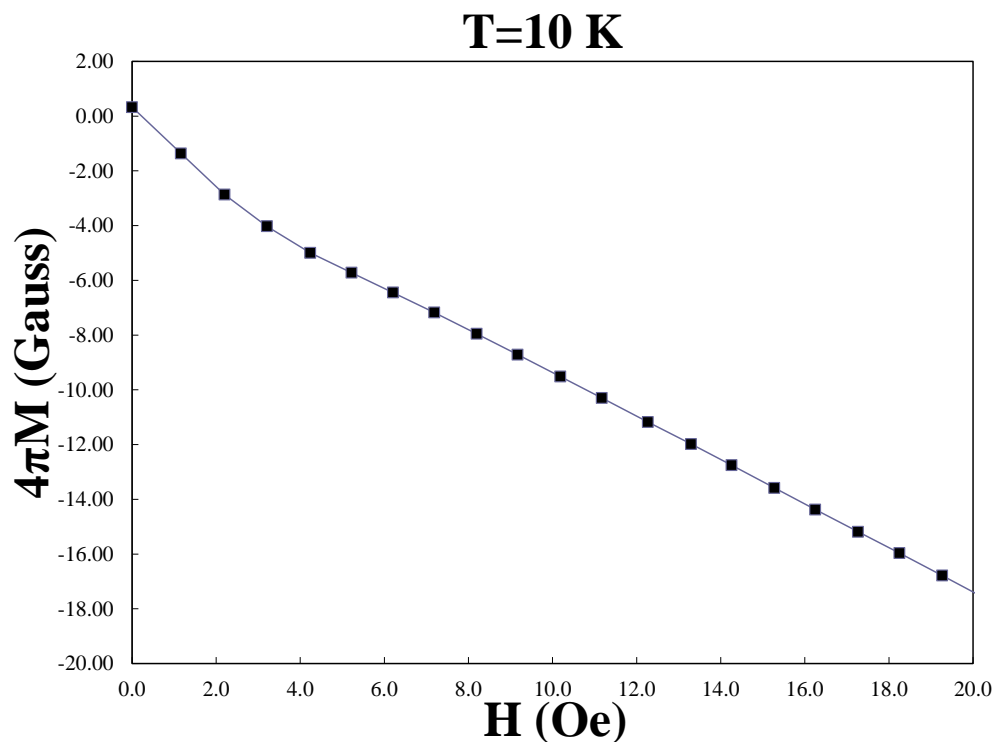
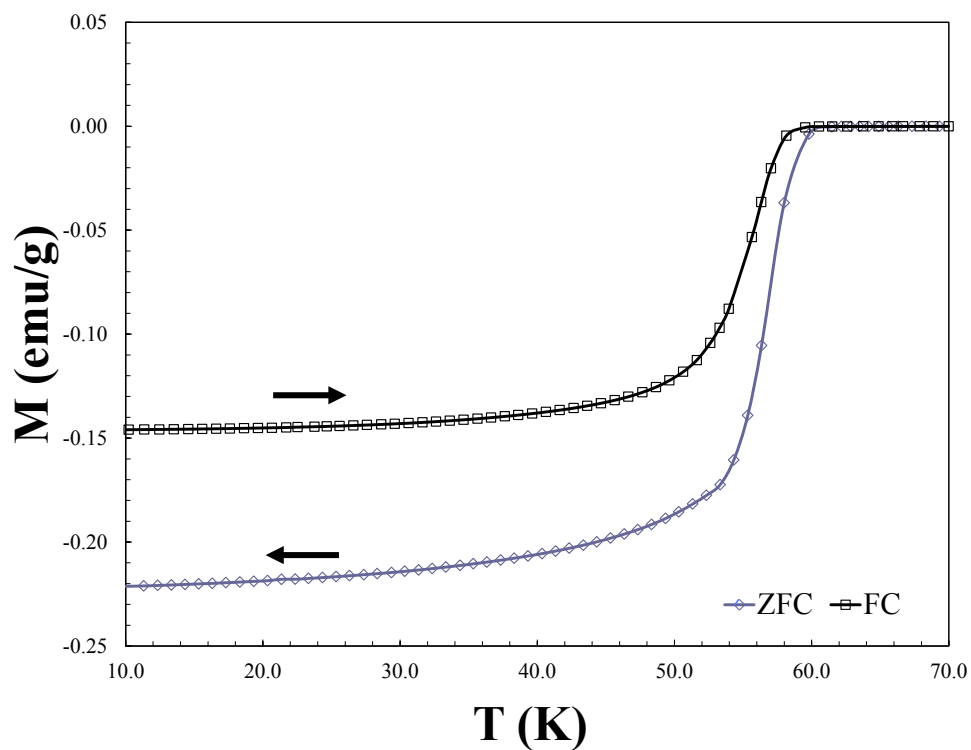


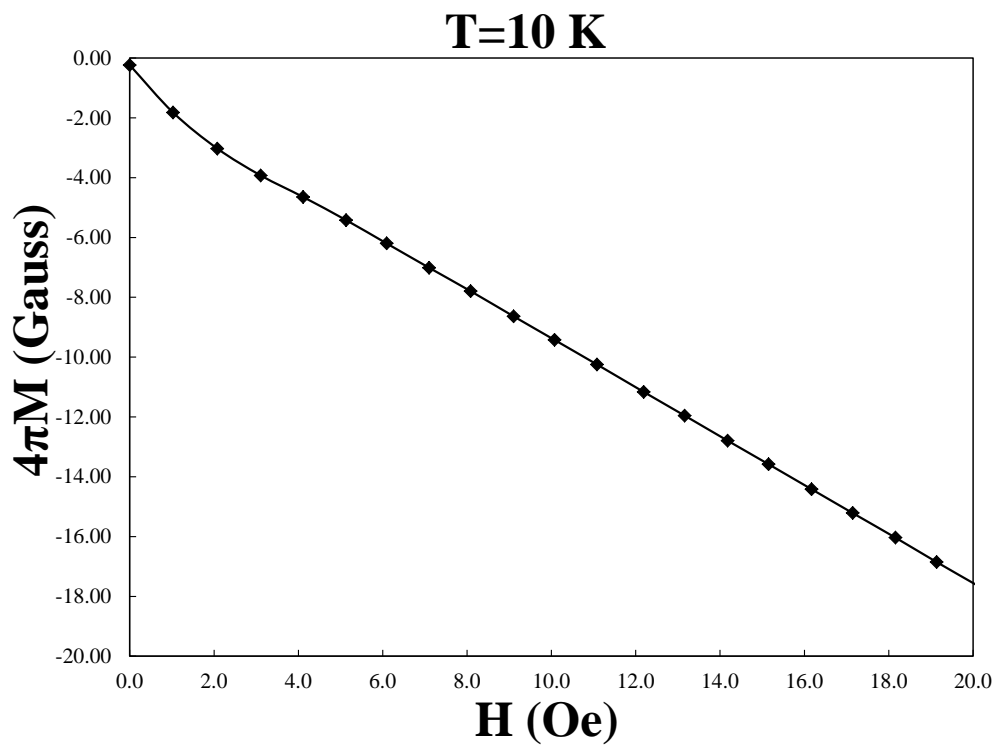
(a) Volume magnetic moment, M , versus applied magnetic field strength, H .



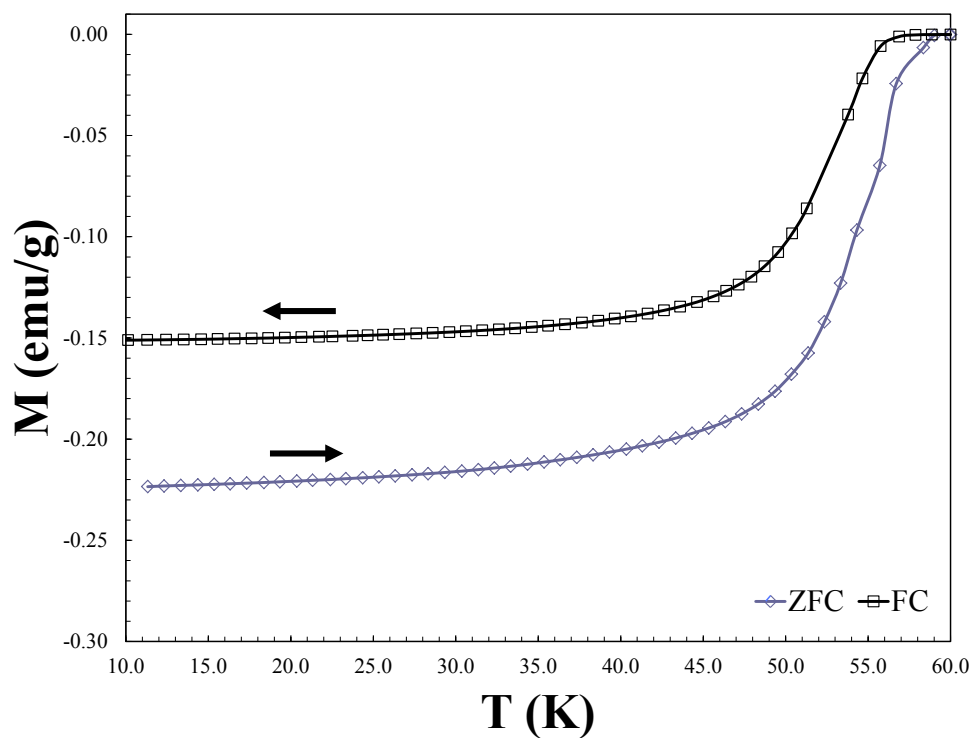
(b) Magnetic moment, M , versus temperature, H .

Figure 15: Magnetic moment measurements for sample BH-5-YBCO-14 with composition $\text{YBa}_2\text{Cu}_3\text{O}_{6.79}$.

(a) Volume magnetic moment, M , versus applied magnetic field strength, H .(b) Magnetic moment, M , versus temperature, H .Figure 16: Magnetic moment measurements for sample BH-5-YBCO-15 with composition $\text{YBa}_2\text{Cu}_3\text{O}_{6.65}$.

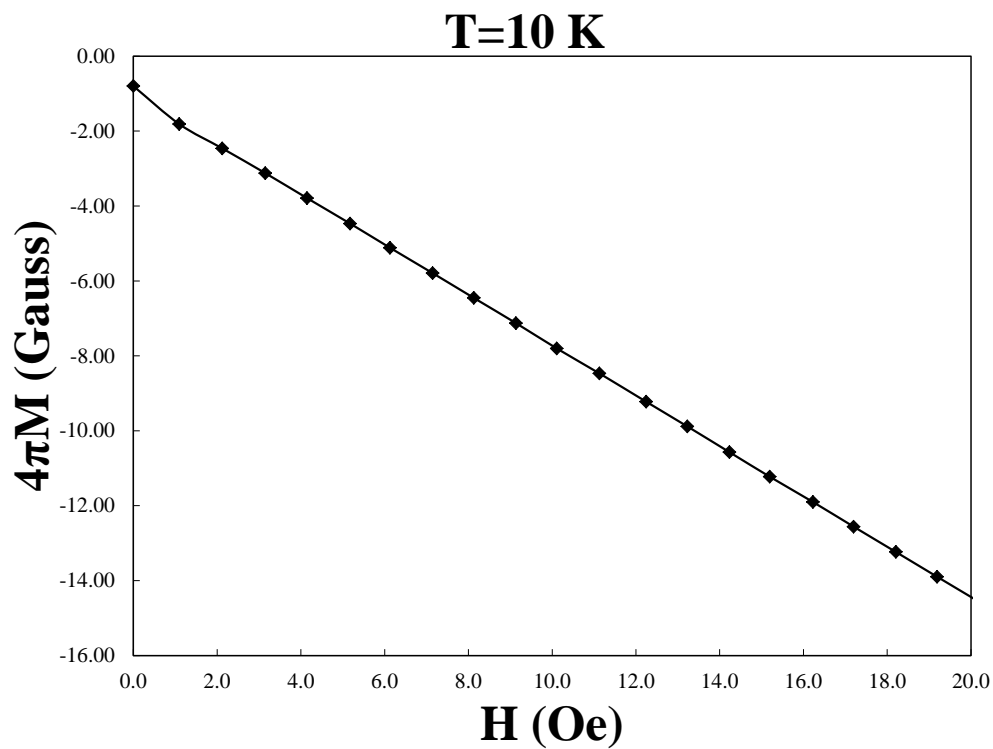


(a) Volume magnetic moment, M , versus applied magnetic field strength, H .

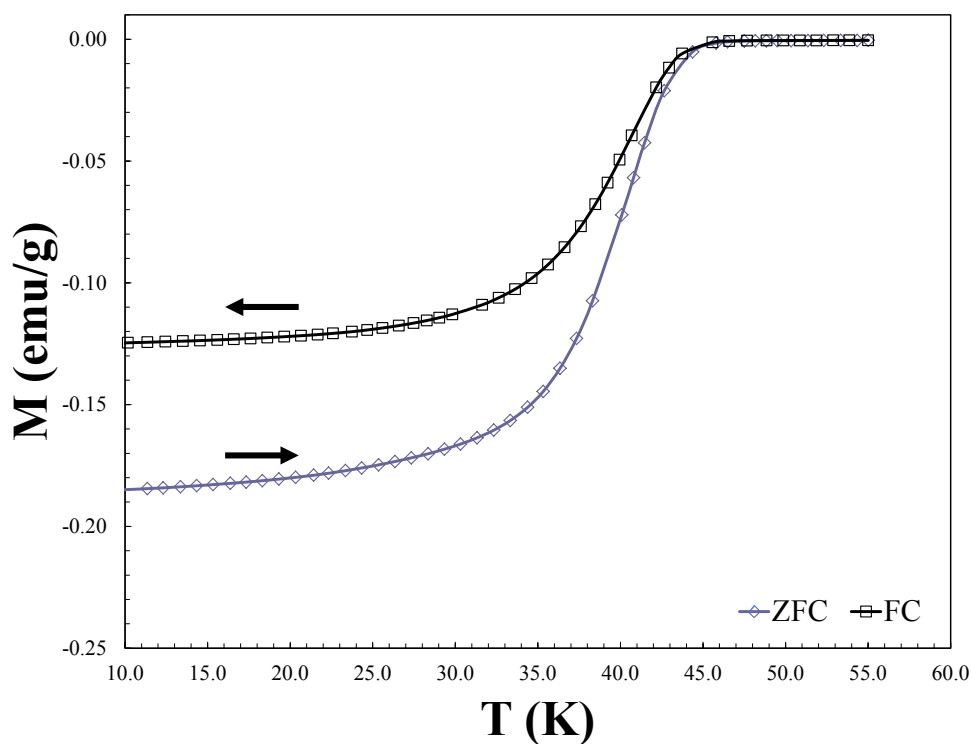


(b) Magnetic moment, M , versus temperature, H .

Figure 17: Magnetic moment measurements for sample BH-5-YBCO-2 with composition $\text{YBa}_2\text{Cu}_3\text{O}_{6.54}$.

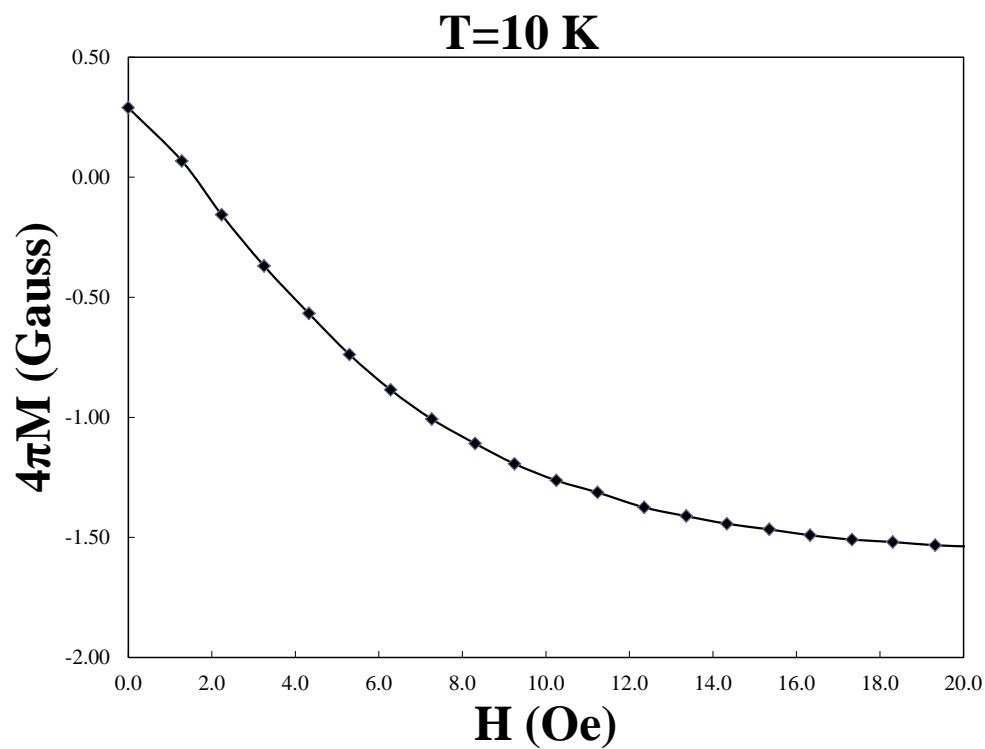


(a) Volume magnetic moment, M , versus applied magnetic field strength, H .

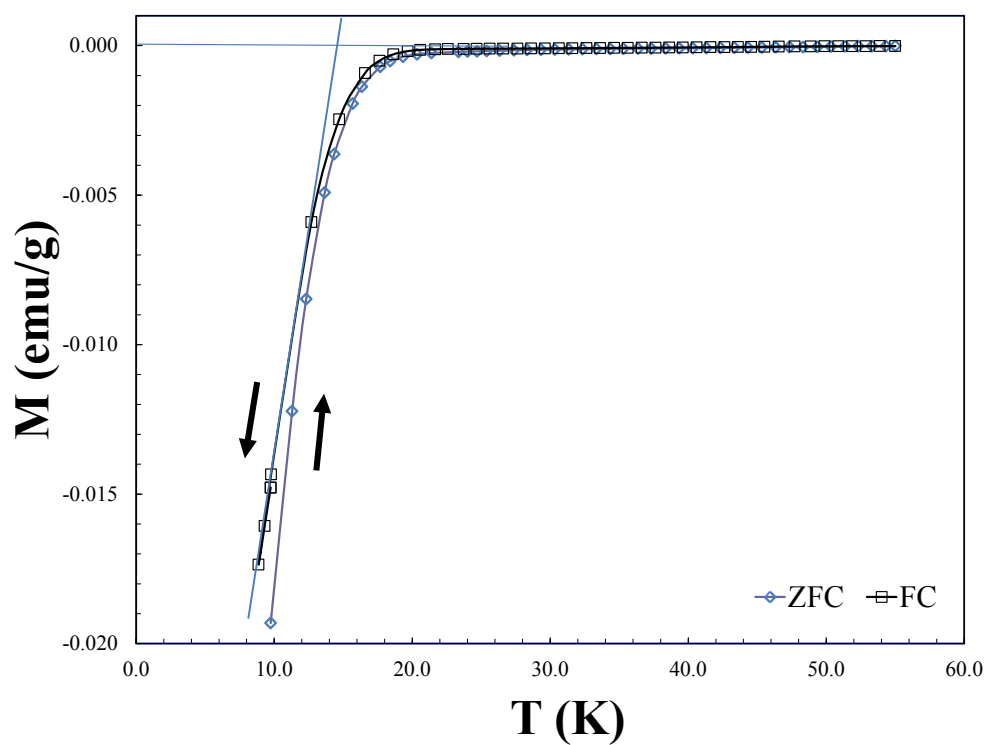


(b) Magnetic moment, M , versus temperature, H .

Figure 18: Magnetic moment measurements for sample BH-5-YBCO-8 with composition $\text{YBa}_2\text{Cu}_3\text{O}_{6.46}$.



(a) Volume magnetic moment, M , versus applied magnetic field strength, H .



(b) Magnetic moment, M , versus temperature, H .

Figure 19: Magnetic moment measurements for sample BH-5-YBCO-6 with composition $\text{YBa}_2\text{Cu}_3\text{O}_{6.33}$.

Table 4: Superconducting transition temperatures for oxygen-deficient samples of $\text{YBa}_2\text{Cu}_3\text{O}_{7-x}$. The transition width of a sample's T_c , ΔT_c , is the temperature range between 50% to 90% and 50% to 10% of the superconducting transition. The superconducting fraction could not be determined for sample with oxygen content of 6.33 because of incomplete superconducting transition in the FC curve of M vs T .

Sample Composition	T_c (K)	ΔT_c	Superconducting fraction (%)
$\text{YBa}_2\text{Cu}_3\text{O}_7$	86	7	69
$\text{YBa}_2\text{Cu}_3\text{O}_{6.79}$	58	8	64
$\text{YBa}_2\text{Cu}_3\text{O}_{6.65}$	52	7	57
$\text{YBa}_2\text{Cu}_3\text{O}_{6.54}$	49	7	59
$\text{YBa}_2\text{Cu}_3\text{O}_{6.46}$	36	7	48
$\text{YBa}_2\text{Cu}_3\text{O}_{6.33}$	<15	–	–

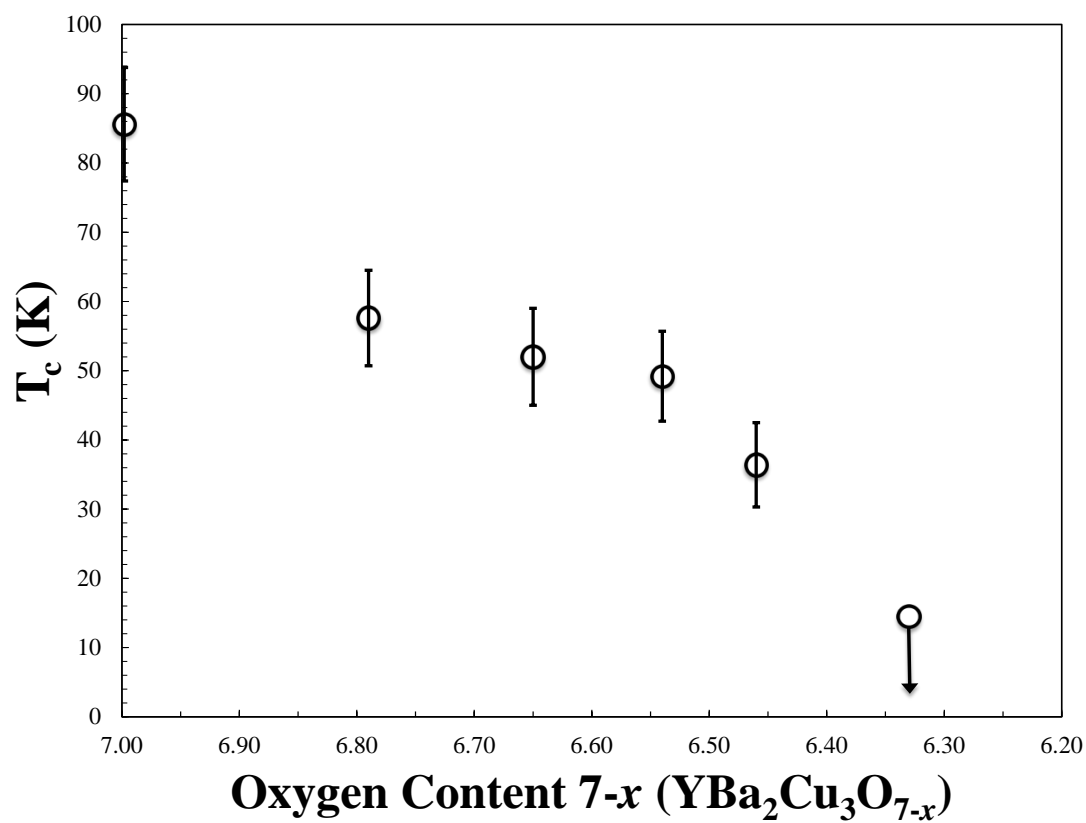


Figure 20: Superconducting transition temperature, T_c , plotted as a function of oxygen composition, $7 - x$, for samples of $\text{YBa}_2\text{Cu}_3\text{O}_{7-x}$. The arrow directed downward for the sample with oxygen content 6.33 indicates that $T_c < 15$.

4 Discussion

4.1 Crystal Structure

The lattice parameters of the samples generally agree with those in the literature for oxygen-deficient samples [30, 31, 33–42]. The lattice parameters in this study are consistently smaller than those in the literature. The value of a is about 0.2% smaller while values of b and c are less than 0.1% smaller than corresponding lattice parameters in the literature. Despite the difference in values, lattice parameters in this study closely fit the trend of increasing a and c and decreasing b with decreasing oxygen content except the sample with oxygen content 6.79. The change in lattice parameters can be explained by the removal of oxygen from the copper-oxygen chains that lie along the orthorhombic $\text{YBa}_2\text{Cu}_3\text{O}_{7-x}$ b -axis [33–35]. As oxygen atoms are removed, the strain energy that keeps the chain direction along the b -axis diminishes. As a result, the difference between the a - and b -axes becomes smaller and smaller, and eventually the structure becomes tetragonal.

The diffraction peaks of (006), (020), and (200) planes are shown in detail in Figure 21 for the six samples. The (006) and (020) peaks are nearly merged in the fully-oxygenated sample, since b is approximately one-third the length of c . The (020) and (200) peaks are clearly separated indicating that $a \neq b$. The fact that the (006) and (020) peaks are nearly merged in the fully-oxygenated sample explains the higher intensity relative to the intensity of the (200) peak. As the oxygen content decreases, the (020) and (006) peaks are separated and the (020) and (200) peaks begin to merge. The (006) peak moved to the left since lattice parameter c increases with reduced oxygen content, while the (020) peak moves to the right as b decreases with reduced oxygen content. This merging of the (200) and (020) peaks indicates that a and b are approaching the same length, therefore suggesting

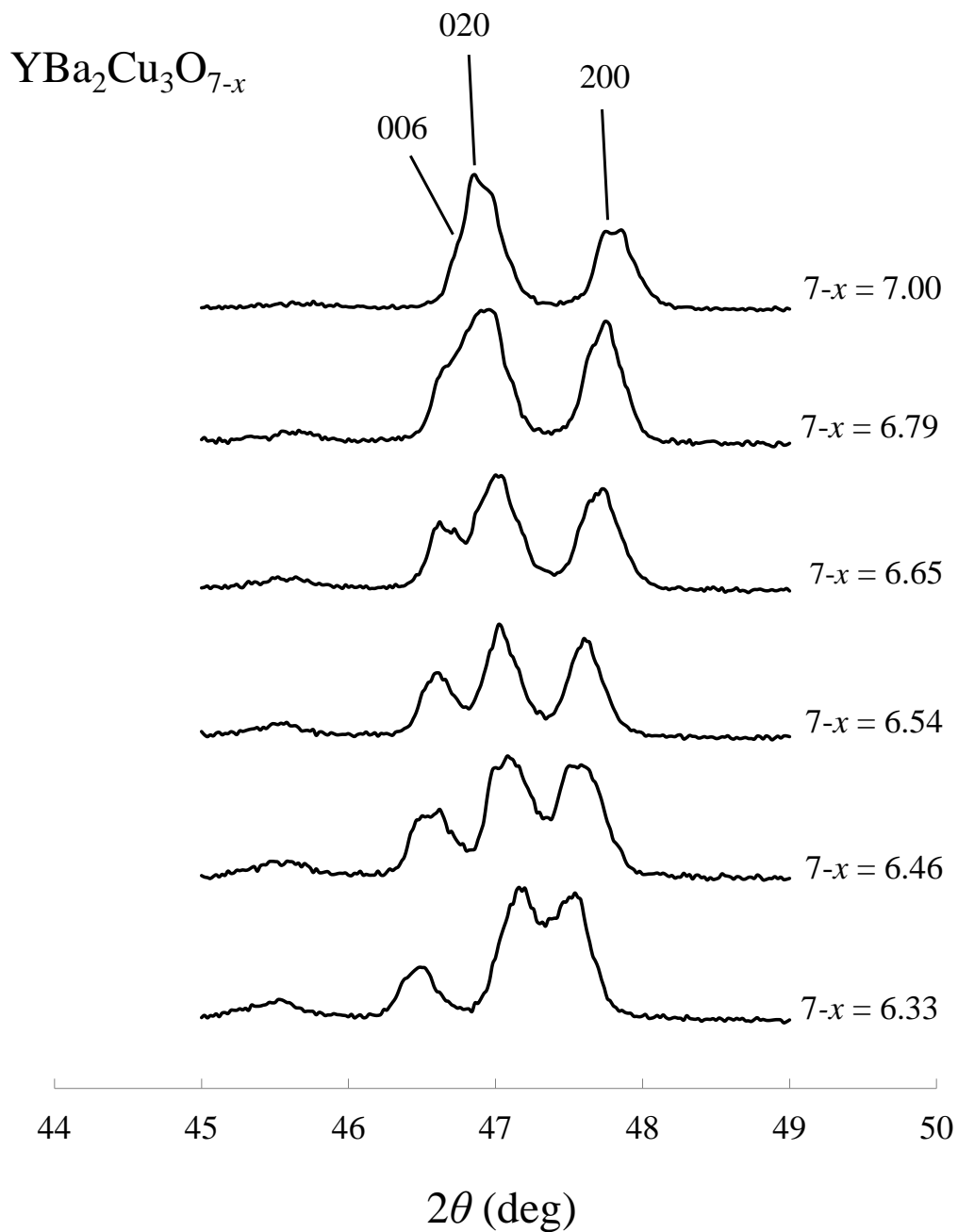


Figure 21: X-ray diffraction peaks (006), (020), and (200) in samples of $\text{YBa}_2\text{Cu}_3\text{O}_{7-x}$ are shown for samples with oxygen content 7.00, 6.79, 6.65, 6.54, 6.46, and 6.33 between $46^\circ < 2\theta < 49^\circ$.

a change in crystal symmetry from orthorhombic to tetragonal. However, the two peaks are still separated in the sample with oxygen content of 6.33. This shows the transition from orthorhombic to tetragonal did not take place at this oxygen content, yet samples with oxygen content of ≈ 6.35 have been reported as having tetragonal crystal structure [34, 35]. The intensities of the (020) and (200) peaks remain about the same as oxygen content is decreased down to 6.33.

The sample with oxygen content 6.79 was found to have a greater value for b than the fully-oxygenated sample, which was the exception to the monotonic decrease in b with decreasing oxygen content. However, the (020) peak in the diffraction pattern of the sample suggests that b is slightly smaller than for the value for the fully-oxygenated sample. The (006) peak is moved to the left, indicating an increased c value. The higher value of b from the Rietveld refinement may be caused by errors in the fitting. The higher value of b for this sample contributed to the large increase in unit cell volume relative to the volume of the fully oxygenated sample.

4.2 Superconducting Properties

Magnetization measurements show superconducting transitions in all of the samples in this study. The theoretical magnetic susceptibility for a superconductor is $\chi = -1$, but two of the samples had values $\chi < -1$ and the remaining four had $\chi > -1$. Values of $\chi < -1$ are believed to result from the porosity in the samples. When a sample is cooled below T_c with $\vec{H} = 0$ (ZFC) to become superconducting, any field subsequently applied to the sample will be shielded by the production of surface currents to maintain $B = 0$ inside the superconductor. As a magnetic field is applied, flux is excluded from the superconductor including the pores, thus leading to a diamagnetic signal that is more negative than what one expects theoretically.

In the FC sequence, the samples initially have normal state magnetization before being cooled in a magnetic field. As the sample is cooled, any non-superconducting fraction or pores in the sample allow flux to remain, which causes a decrease in the magnitude of the overall magnetization. The fact that $-1.0 \lesssim \chi \lesssim -0.7$ for samples with the oxygen contents of 6.79, 6.65, 6.54, and 6.46 indicates those samples contain a significant non-superconducting fraction. For the sample with oxygen content 6.33, the susceptibility is an order of magnitude smaller than those of the other samples. The plot of M versus H reveals a deviation from linear behavior, which indicates an extremely low critical magnetic field. Furthermore, the M versus T plot of this sample shows that the superconducting transition is not complete down to 10K.

The data clearly indicate that T_c decreases as oxygen is removed from $\text{YBa}_2\text{Cu}_3\text{O}_{7-x}$, and the superconducting volume also decreases with oxygen content. Neutron diffraction measurements indicate this trend occurs as a consequence of fewer charge carriers because oxygen is being removed at the copper-oxygen chain sites [34, 35]. What can be described as a plateau in T_c versus oxygen content between 6.50 and 6.75 resembles that reported in the literature [34, 35]. The existence of a plateau might be a result of oxygen ordering of the copper-oxygen chains in a sequence of occupied and unoccupied oxygen sites. This oxygen ordering has previously been observed in electron diffraction measurements [46–48]. The T_c values are consistent with those reported in the literature except for the sample with oxygen content 6.79. The T_c for the sample with oxygen content 6.79 is as much as 19K lower than values reported in the literature for that oxygen content [35]. This suggests that the sample used for magnetic measurement likely had a lower oxygen content than what was determined from weight loss measurements.

Discrepancies between lattice parameters in this study and those in the literature may have been caused by the lack of oxygen in the original sample, which was assumed

to have an oxygen content of 7.00 ± 0.03 . Evidence of oxygen inhomogeneity in this sample is seen in the M versus H plot as a “kink” toward the superconducting transition completion. Oxygen inhomogeneity in the original, fully-oxygenated sample may have resulted from the large batch size ($\approx 12\text{g}$). Consequently, the calculation of oxygen content assuming that the original sample was fully oxygenated throughout would be propagated through the oxygen-deficient samples. If the oxygen content of samples in this study are decreased by 0.05 to account for the original sample having an oxygen content of 6.95, the lattice parameters are closer to values in the literature for samples with similar oxygen content. Shifting the data in this manner maintains the consistency between T_c values in this study and those in the literature.

5 Conclusion

A set of $\text{YBa}_2\text{Cu}_3\text{O}_{7-x}$ samples were made by quenching fully-oxygenated samples after high-temperature annealing. The oxygen contents were 6.79, 6.65, 6.54, 6.46, and 6.33. The lattice parameters a and c were observed to monotonically increase while b nearly monotonically decreases with decreasing oxygen content. All samples had orthorhombic symmetry; hence no orthorhombic to tetragonal phase transition was observed. The lattice parameters of our samples are consistently smaller than those reported in the literature. Magnetization measurements indicated that T_c as well as superconducting volume fraction decreased as oxygen content decreased. Most T_c values were consistent with the literature for samples with similar oxygen content. Similar to results reported in the literature [34, 35], a plateau in T_c values between samples with oxygen contents $6.50 \lesssim 7 - x \lesssim 6.75$ was observed, possibly due to the ordering of the oxygen atoms at the copper-oxygen chain sites. Our results for crystal structure and superconductivity in $\text{YBa}_2\text{Cu}_3\text{O}_{7-x}$ are consistent with the model describing the decrease in T_c as a result of oxygen being removed from the copper-oxygen chain sites. The discrepancies in lattice parameters for samples in this study with those reported in the literature are likely caused by the original sample not being fully oxygenated, the actual oxygen content may be approximately 6.95 instead of 7.00. To ensure samples are fully oxygenated, synthesis of $\text{YBa}_2\text{Cu}_3\text{O}_7$ samples by the procedure in this study should be limited to a batch size less than 10 g. Other methods of creating oxygen-deficient samples should be considered for future studies on the normal state magnetization of $\text{YBa}_2\text{Cu}_3\text{O}_{7-x}$. Instead of annealing $\text{YBa}_2\text{Cu}_3\text{O}_7$ in air to prepare oxygen-deficient samples, annealing could be done at a constant temperature with controlled argon-oxygen mixtures.

References

- [1] J. Biscaras, B. Leridon, D. Colson, A. Forget, and P. Monod, Phys. Rev. B **85**, 134517 (2012).
- [2] H. K. Onnes, Leiden Communications, **120b**, **122b**, **124c**, (1911).
- [3] W. Meissner and R. Ochsenfeld, Naturwiss. **21**, 787 (1933).
- [4] F. London and H. London, "The electromagnetic equations of the supraconductor," Proc. Roy. Soc. **A149**, 71 (1935).
- [5] V.L. Ginzburg and L.D. Landau, Zh. Eksp. Teor. Fiz. **20**, 1064 (1950).
- [6] J. Bardeen, L.N. Cooper and J.R. Schrieffer, "Theory of superconductivity," Phys. Rev. **108**, 1175 (1957).
- [7] A. Bourdillon and N. X. Tan Bourdillon, *High Temperature Superconductors: Processing and Science*, Academic Press, San Diego, CA 92101-4311, 1994.
- [8] C. Kittel, *Introduction to Solid State Physics*, John Wiley and Sons, Inc., 8th edition, 2005.
- [9] R. Meservey and B. B. Schwartz, Superconductivity Vol. 1 (R.D. Parks, eds.), Marcel Dekker Inc., New York, 1969.
- [10] P. Townsend, J. Sutton, Phys. Rev. **128-2**, 591-595 (1962).
- [11] H. Frölich, Phys. Rev. **79**, 845 (1950).
- [12] E. Maxwell, Phys. Rev. **78**, 477 (1950).
- [13] Reynolds, Serin, Wright, and Nesbitt, Phys. Rev. **78**, 487 (1950).

- [14] R. Serway and C. Vuille, *College Physics*, Brooks/Cole Cengage Learning, Boston, MA, 8th edition, 2012.
- [15] A. C. Rose-Innes and E. H. Rhoderick, *Introduction to Superconductivity*, BPC Wheatons, Exeter, 2nd edition, 1994
- [16] W. Tuyn and H. K. Onnes, Communications of the Physical Laboratory, University of Leiden, **174a**, 21 (1926).
- [17] W. Tuyn and H. K. Onnes, J. Franklin Inst. **201**, 379 (1926).
- [18] T. C. Keeley, K. Mendelssohn, and J. R. Moore, Nature **134**, 773 (1934).
- [19] W. J. de Haas and J. M. Casimir-Jonker, Nature **135**, 30 (1935).
- [20] F. G. A. Tarr and J. O. Wilhelm, Can. J. Res. **12**, 265 (1935).
- [21] A. A. Abrikosov, Doklady Akademii Nauk SSSR86, 489 (1952).
- [22] J. G. Bednorz and K. A. Müller, Z. Phys. B - Condensed Matter **64**, 189 (1986).
- [23] J.R. Gavaler, M.A. Janocko, C. J. Jones, Appl. Phys. Lett. **23-8**, 480 (1973).
- [24] M. K. Wu, J. R. Ashburn, C. J. Torng, P. H. Hor, R. L. Meng, L. Gao, Z. J. Huang, Y. Q. Wang, and C. W. Chu, Phys. Rev. Lett. **58**, 908 (1987).
- [25] H. Maeda, Y. Tanaka, M. Fukutomi, T. Asano, Jpn. J. Appl. Phys. **27**, 209 (1988).
- [26] Z.Z. Sheng, A.M. Hermann, Nature. **332**, 138 (1988).
- [27] P. Dai, B.C. Chakoumakos, G.F. Sun, K.W. Wong, Y. Xin, and D.F. Lu, Physica C. **243** No. 3&4, 201-206 (1995).

- [28] Jin, Sungho. Processing and Properties of High-Tc Superconductors. Songapore: World Scientific, 1993.
- [29] Zhi-An Ren, Guang-Can Che, Xiao-Li Dong, Jie Yang, Wei Lu, Wei Yi, Xiao-Li Shen, Zheng-Cai Li, Li-Ling Sun, Fang Zhou and Zhong-Xian Zhao, EPL 2008 EPL **83**, 17002 (2008).
- [30] Y. Zhu, A. R. Moodenbaugh, M. Suenaga, and J. Tafto, Physica C **167**, 363 (1990).
- [31] J. D. Jorgensen, M. A. Beno, D. G. Hinks, L. Soderholm, K. J. Volin, C. U. Segre, K. Zhang, and M. S. Kleefisch, Phys. Rev. B **36**, 3608 (1987).
- [32] J. J. Capponi, C. Chailout, A. W. Hewat, P. Lejay, M. Marezio, N. Nguyen, B. Raveau, J. L. Soubeyroux, J. L. Tholence and R. Tournier, Europhys. Lett. **3**, 1301 (1987).
- [33] J. M. Tranquada, S. M. Heald, A. R. Moodenbaugh, and Youwen Xu, Phys. Rev. B **38**, 8893 (1988).
- [34] R. J. Cava, A. W. Hewat, E. A. Hewat, B Batlogg, M. Marezio, K. M. Marezio, K. M. Rabe, J. J. Krajewski, W. F. Peck, Jr., and L. W. Rupp, Jr., Physica C **165**, 419 (1990).
- [35] J. D. Jorgensen, B. W. Veal, A. P. Paulikas, L. J. Nowicki, G. W. Crabtree, H. Claus, and W. K. Kwok, Phys. Rev. B **41**, 1863 (1990).
- [36] R. J. Cava, B. Batlogg, C. H. Chen, E. A. Rietman, S. M. Zahurak, and D. Werder, Phys. Rev. B **36**, 5719 (1987).
- [37] J. D. Jorgensen, B. W. Veal, W. K. Kwok, G. W. Crabtree, A. Umezawa, L. J. Nowicki, and A. P Paulikas, Phys. Rev. B **36**, 5731 (1987).

- [38] Y. Nakazawa, M. Ishikawa, *Physica C* **158**, 381 (1989).
- [39] S. C. Tidrow, D. M. Pierce, A. Tauber, W. D. Wilber, R. D. Finnegan, D. W. Eckart, *J. Supercond.* **11**, 219 (1998).
- [40] S. Degoy, J. Jimenez, P. Martin, O. Martinez, A. C. Prieto, D. Chambonnet, C. Audry, C. Belouet, J. Perriere, *Physica C.* **251**, 291 (1996).
- [41] J. Ye, K. Nakamura, *Phys. Rev. B* **48**, 7554 (1993).
- [42] Kh. A. Ziq, *Supercond. Sci. Technol.* **14**, 30 (2001).
- [43] H. M. Rietveld, *J. Appl. Cryst.* **2**, 65 (1969).
- [44] B. D. Cullity, *Elements of X-ray Diffraction*, Addison-Wesley Publishing Company, Inc., 1956.
- [45] R. J. Cava, B. Batlogg, S. A. Sunshine, T. Siegrist, R. M. Fleming, K. Rabe, L. F. Schneemeyer, D. W. Murphy, R. B. van Dover, P. K. Gallagher, S. H. Glarum, S. Nakahara, R. C. Farrow, J. J. Krajewski, S. M. Zahurak, J. V. Waszczak, J. H. Marshall, P. Marsh, L. W. Rupp Jr., W. F. Peck, E. A. Rietman *Physica C* **153-155**, 560 (1988).
- [46] G. Van Tendeloo, H. W. Zandbergen, and S. Amelinckx, *Solid State Commun.* **63**, 89 (1987).
- [47] D.J. Werder, C.H. Chen, R.J. Cava and B. Batlogg, *Phys. Rev. B* **37**, 2317 (1988).
- [48] R. M. Fleming, L. F. Schneemeyer, P. K. Gallagher, B. Batlogg, L. W. Rupp, and J. V. Waszczak, *Phys. Rev. B* **37**, 7920 (1988).

A Material List

Table 5: List of starting materials used for the synthesis of $\text{YBa}_2\text{Cu}_3\text{O}_7$ and for X-ray diffraction measurements.

Element or Compound	Source	Purity
BaCO_3	J. T. Baker, Lot #408877	-
CuO	Alfa Aesar, Lot # 10700	99.995%
Y_2O_3	REacton, Batch #R4563	4N
Si	Alfa Aesar, Lot # 5004L22V	5N
